IMAGING CRUSTAL STRUCTURE BENEATH TEXAS FROM RECEIVER FUNCTIONS

A Thesis Presented to

the Faculty of the Department of Earth and Atmospheric Sciences

University of Houston

In Partial Fulfillment

of the Requirement for the Degree

Master of Science

By

Xixi Wang

December 2013

IMAGING CRUSTAL STRUCTURE BENEATH TEXAS FROM RECEIVER FUNCTIONS

Xixi Wang

APPROVED:

Dr. Aibing Li
Department of Earth and Atmospheric Sciences

Dr. William Sager
Department of Earth and Atmospheric Sciences

Dr. Dale Bird
Bird Geophysical

Dean, College of Natural Sciences and Mathematics

ACKNOWLEDGEMENTS

Foremost, I would like to express my sincere gratitude to my advisor and mentor Dr. Aibing Li for the continuous advising on my Master's study and research. Her guidance helped me throughout of my research and writing of this thesis. I deeply appreciate her kindness and patience throughout the two years.

I would also like to thank my thesis committee members, Dr. Dale Bird and Dr. William Sager, for their encouragement, insightful comments and questions on my Master's research.

My thanks also go to my fellow group members and classmates, especially Duo Yuan, Lun Li, Riddhi Dave, Yao Yao, who provided me kind help and encouragement during my thesis research and Master's study.

Last but not least, I would like to thank my family and friends for their endless love and support throughout my Master's study in the United States.

IMAGING CRUSTAL STRUCTURE BENEATH TEXAS FROM RECEIVER FUNCTIONS

An Abstract of a Thesis Presented to

the Faculty of the Department of Earth and Atmospheric Sciences

University of Houston

In Partial Fulfillment

of the Requirement for the Degree

Master of Science

By

Xixi Wang

December 2013

ABSTRACT

The shallow crust in Texas has been intensively investigated through seismic exploration for hydrocarbon resources. However, the deep crustal structure of Texas is not well understood. This thesis aims to illuminate crustal structure beneath Texas using P receiver functions at 66 stations of the Transportable Array. Individual receiver functions were calculated and stacked by station using both common conversion point (CCP) and H-κ stacking methods to image the Moho depth variation. Results from the two methods show similarities in the central and southern part of the Ouachita belt. The Moho depth along the Ouachita belt is generally among 35-40 km, and the deepest Moho appears in the Llano uplift area with a thickness approaching 45 km, while it is thinning towards the southern end of the Ouachita belt to about 35 km. In addition, the V_p/V_s ratios calculated using the H-κ method are high (above 1.9) for a couple of stations near the southeastern side of the Ouachita belt, which may correspond to the volcanic material beneath the southern margin of Laurentia and thus imply the ancient rifting activity. However, the Moho structure beneath the Gulf coast plain was not well resolved due to interference between the primary Moho conversion and the multiples from the base of the sedimentary layer. Nevertheless, a Ps phase with delay time varying from 0.5 to 4 s was identified at several stations near

the coastline, which appears to be the Ps conversion from the interface between sediments and crystalline basement.

CONTENTS

List of Figures

CHAPTER 1

INTRODUCTION

Texas is the major province of oil and gas exploration in North America. The evolution of Gulf of Mexico and rifting of Texas Gulf coast have created a natural nursery for sedimentary loading. Since the early 20th century, intensive efforts have been made for the exploration of hydrocarbon deposits in the adjacencies of Texas Gulf coast (Figure 1). It is well established that the coastal plain is overlaid by massive Mesozoic and Cenozoic deposits with greatest thickness of 15 km approaching the coastline (Colle et al., 1952). However, the thick accumulations of sediments have obscured the investigation of deeper earth structure since regular reflection seismic surveys cannot penetrate the thick sedimentary rocks and resolve the crystalline crust. Therefore, techniques using teleseismic energy and potential field data, which are less effected by shallow layers, become important in studying of deep crustal structure beneath Texas.

One of the commonly used methods to investigate the crust and upper mantle structure from teleseismic body wave is receiver function, a time series computed from three-component seismograms that reflect Earth structures near the receiver. In my thesis, P-receiver functions were

calculated to image the lateral variation of Moho depth beneath southeastern-central Texas extends from the coastal plain to the Llano uplift area (Figure 2).

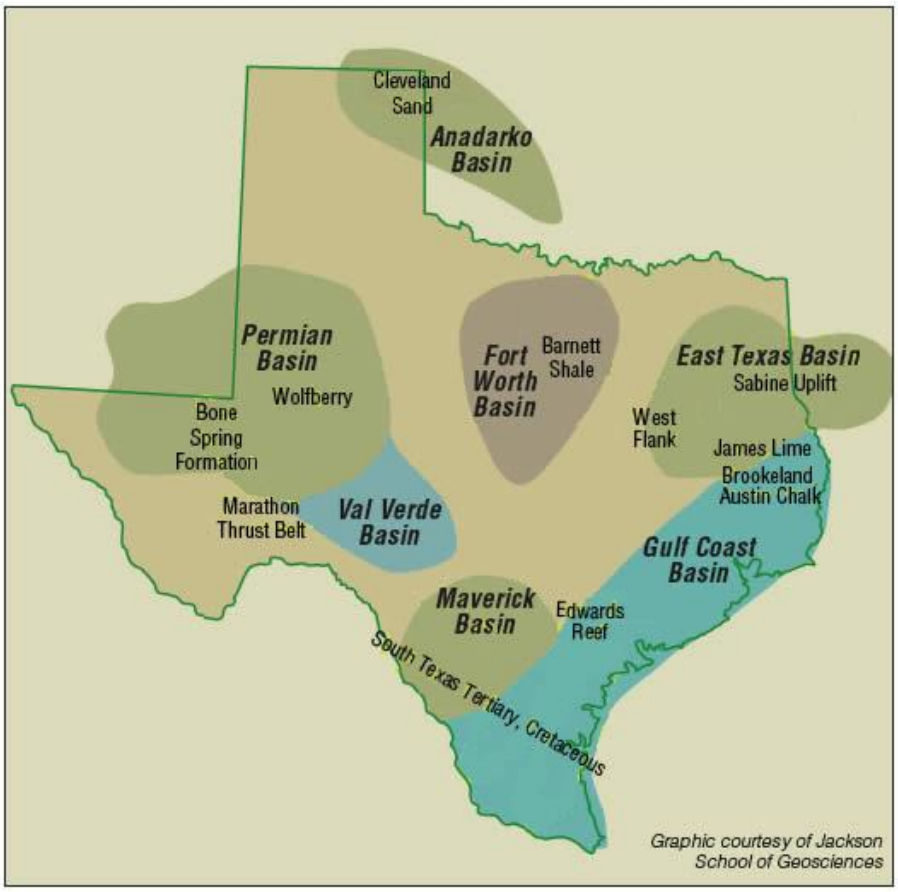

Figure 1. The major oil and gas producing basins of Texas (Modified from Jackson School of Geosciences, the University of Texas at Austin, 2008)

I computed P-receiver functions from teleseismic data recorded at the broadband stations of the USArray Transportable Array (TA), which have stations spacing of 70 km and have produced many of seismograms. First, teleseismic waveforms are processed to calculate individual receiver functions for all selected earthquakes at all the broadband stations. Then, the receiver functions for each station are stacked using two different

algorithms. The Moho depths beneath all the stations can be estimated using the stacked receiver functions. By analyzing stations covering several tectonic zones of southeastern Texas, lateral variation of the Moho depth and V_p/V_s ratios can be mapped out throughout the study area (Figure 2). The results from this study reveal the regional structural variation and give insights to the tectonics of Texas area and the evolution of the Gulf of Mexico.

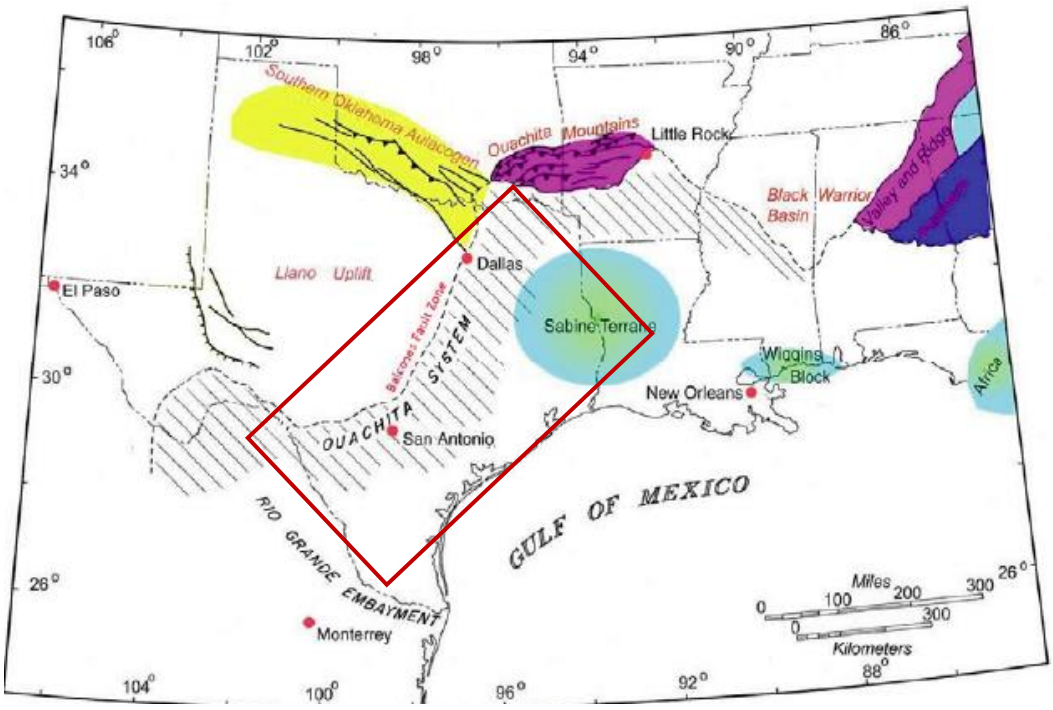

Figure 2. Modern tectonic features of Texas. The proposed study area is enclosed by the red box (Modified from Speckien, 2012)

The following chapters of this thesis are briefly described here.

Chapter 2 introduces the regional tectonic and geological settings of Texas area, as well as the previous works in this region.

Chapter 3 provides basic knowledge of the P receiver function, CCP stack and H-κ method that are adopted in this study.

Chapter 4 explains the data origin in detail, showing the spatial distribution of the utilized broadband stations and events that are selected to calculate the individual receiver functions.

Chapter 5 shows the results obtained from P receiver function methods across the southeastern Texas. The results are presented in a profile across major tectonic boundaries, and in maps illustrating Moho depth variation in the study area.

Chapter 6 compares the results with previous studies and discusses interesting features in the observations.

The conclusions are presented in Chapter 7.

CHAPTER 2

GEOLOGICAL SETTINGS AND PREVIOUS STUDIES

2.1 Texas Geology

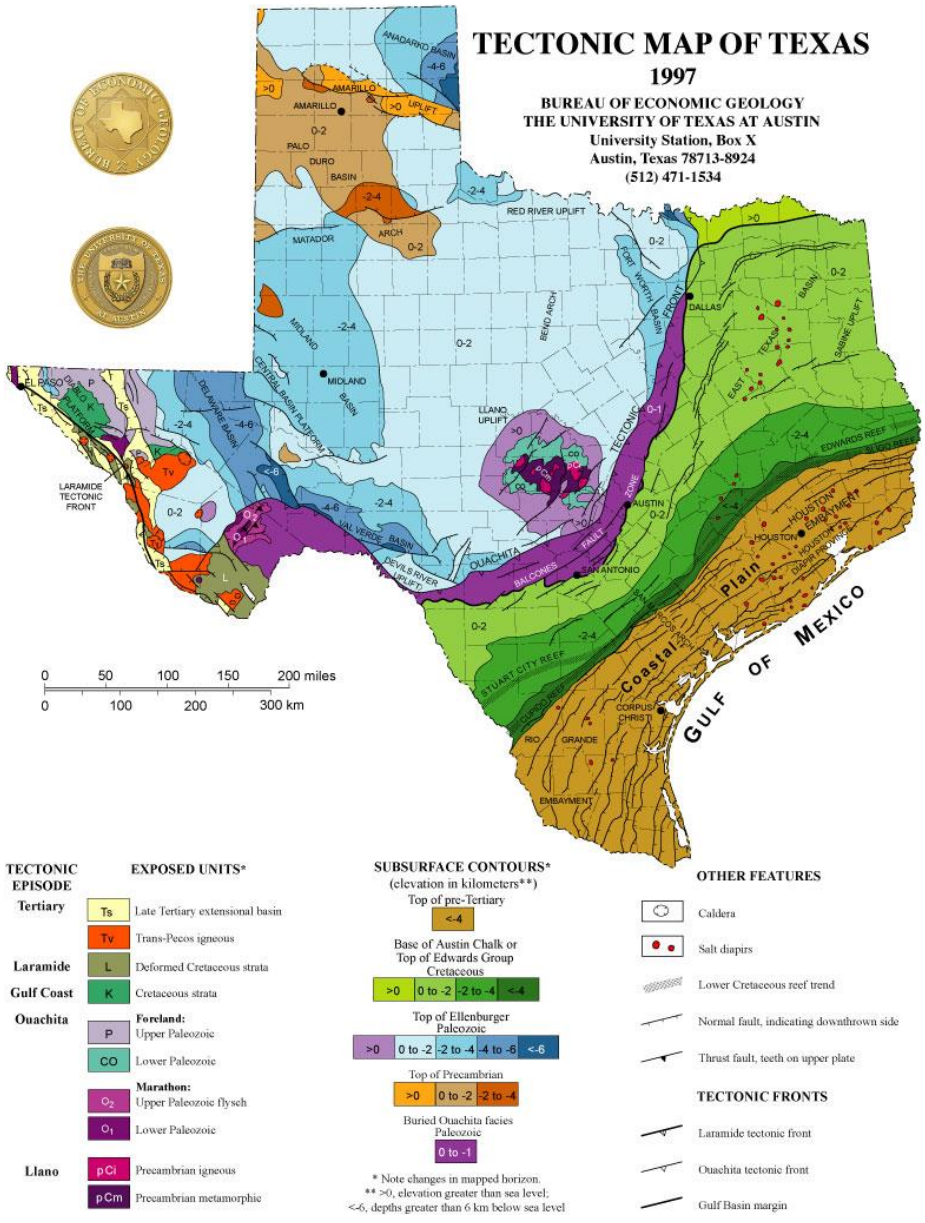

Figure 3. Tectonic map shows major structural features of Texas, including tectonic fronts that mark edges of major basins and former orogenic belts. Crosscutting relations show the relative ages of features (Bureau of Economic Geology, The University of Texas at Austin, 1997)

Texas underwent three principal tectonic periods during the formation of Laurentia as well as the assembly and breakup of Pangaea, comprising two Wilson cycles (Huerta and Harry, 2012). These activities have formed three major tectonic provinces, The Grenville province, the Ouachita belt, and the Gulf coastal plain (Figure 3).

During the formation of Rodinia around 1.1Ga, partial deformation of the crust occurred due to the collisional Grenville orogeny along the southern margin of Laurentia (Dickinson, 2009; Mosher, 2008). One prominent feature as a result of this cycle is the Llano uplift in central Texas.

In early Paleozoic time, Laurentia rifted apart during the breakup of Rodinia, leading to the formation of pre-Ouachita passive margin (Thomas, 1991). Subsequently, the Ouachita orogenic belt formed along the suture zone in the collision of Gondwana and Laurentia around 300Ma during assembly of Pangaea (Dickinson, 2009). This period is recorded in the segments exposed in Arkansas, Oklahoma and Marathon region of Texas, while much portion of the Ouachita belt is covered by postorogenic sediments (Thomas and Viele, 1983).

Beginning around 200 Ma, Pangaea split apart along the western edge of the Gulf of Mexico while the South American plate and the Yucatan

block pulled away from the North American plate (Bird et al., 2005; Dickinson, 2009). This process established the formation of modern continental margin and the opening of modern Atlantic Ocean, isolating the North American, South American, and African continents and finally delineating the southern margin of North America (Dunbar and Sawyer, 1987; Dickinson, 2009).

The Llano uplift of central Texas forms part of the discontinuous belt of Grenville province that extends more than 2000km from Canada to southern Mexico (Garrison, 1981; Hynes and Rivers, 2010). It exposes the core of the Mesoproterozoic orogenic belt that formed along the southern margin of Laurentia during Grenville time (Mosher, 2008). The occurrence and distribution of diverse types of rocks, including polydeformed metamorphic rocks, syn- to post-tectonic intruded granites aged ~1200Ma, imply substantial tectonic history of collision orogeny (Carlson et al., 2007; Mosher, 2008).

Mosher (2008) proposed a model explaining the evolution of Llano uplift associated with Grenville orogenesis, involving the plate tectonic process of subduction, collision and convergence. The model suggests the southwestward subduction of the Laurentia continent, accompanying

retrodeformation and buoyance-driven uplift of crustal segments within the subduction zone and leading to orogenic thickening of Laurentia at Coal Creek domain from the overriding of collided crust, which resulted in high-pressure metamorphism of continental crustal at depth (Figure 4A and B). Further deformation occurred along with ongoing northward transform at higher crust level (Figure 4C). Slab break-off enhanced the uplift and caused depressurization to high-pressure rocks. Subsequent asthenosphere upwelling resulted in continental crust thinning and caused underplating of basaltic magmas (Figure 4D). Continued subduction along strike of the Llano after collision yielded a contractional stress field during the later intrusion, inducing further shortening in the Llano region (Figure 4E).

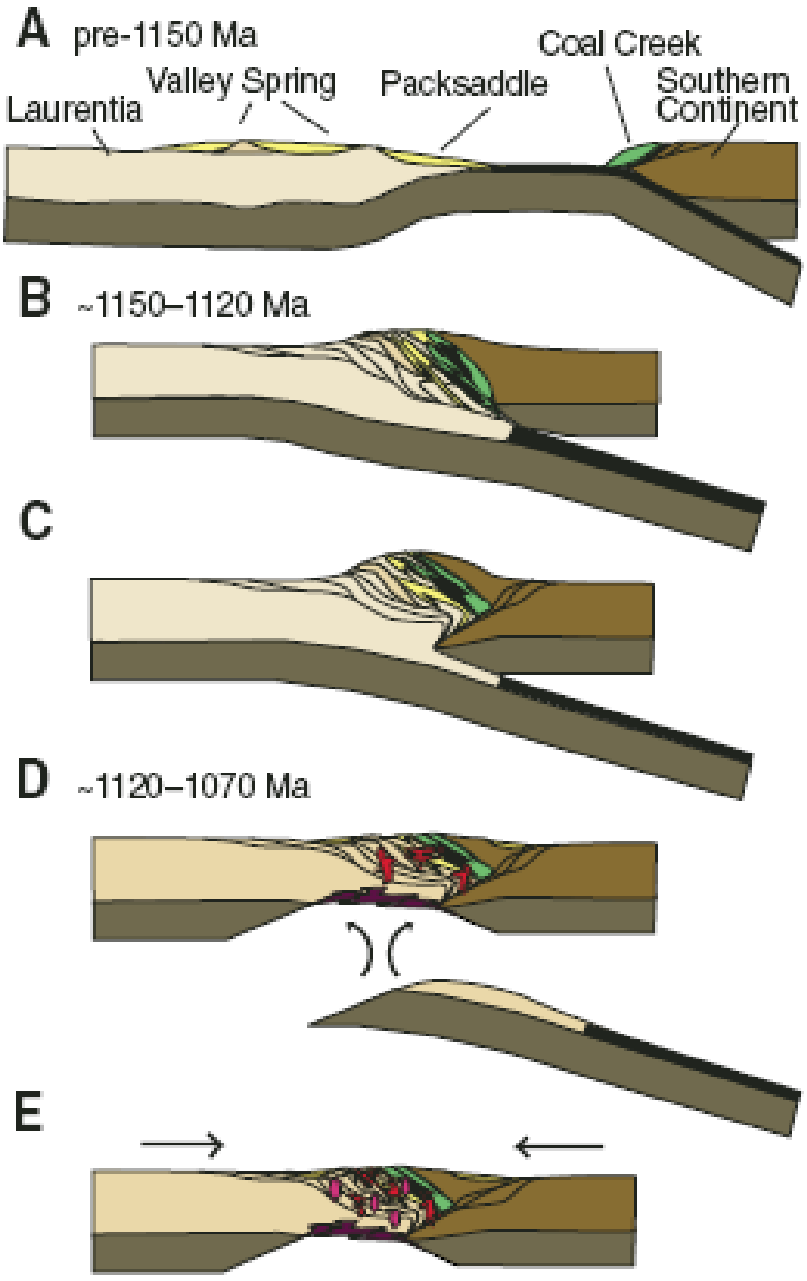

Figure 4. Tectonic model for Grenville orogeny, showing evolution of Llano uplift (Mosher, 2008)

The spatial association and dependency between the continental breakup and preexisting orogeny are well presented in the evolution of Ouachita orogeny and Gulf coast margin (Figure 5) (Huerta and Harry, 2012).

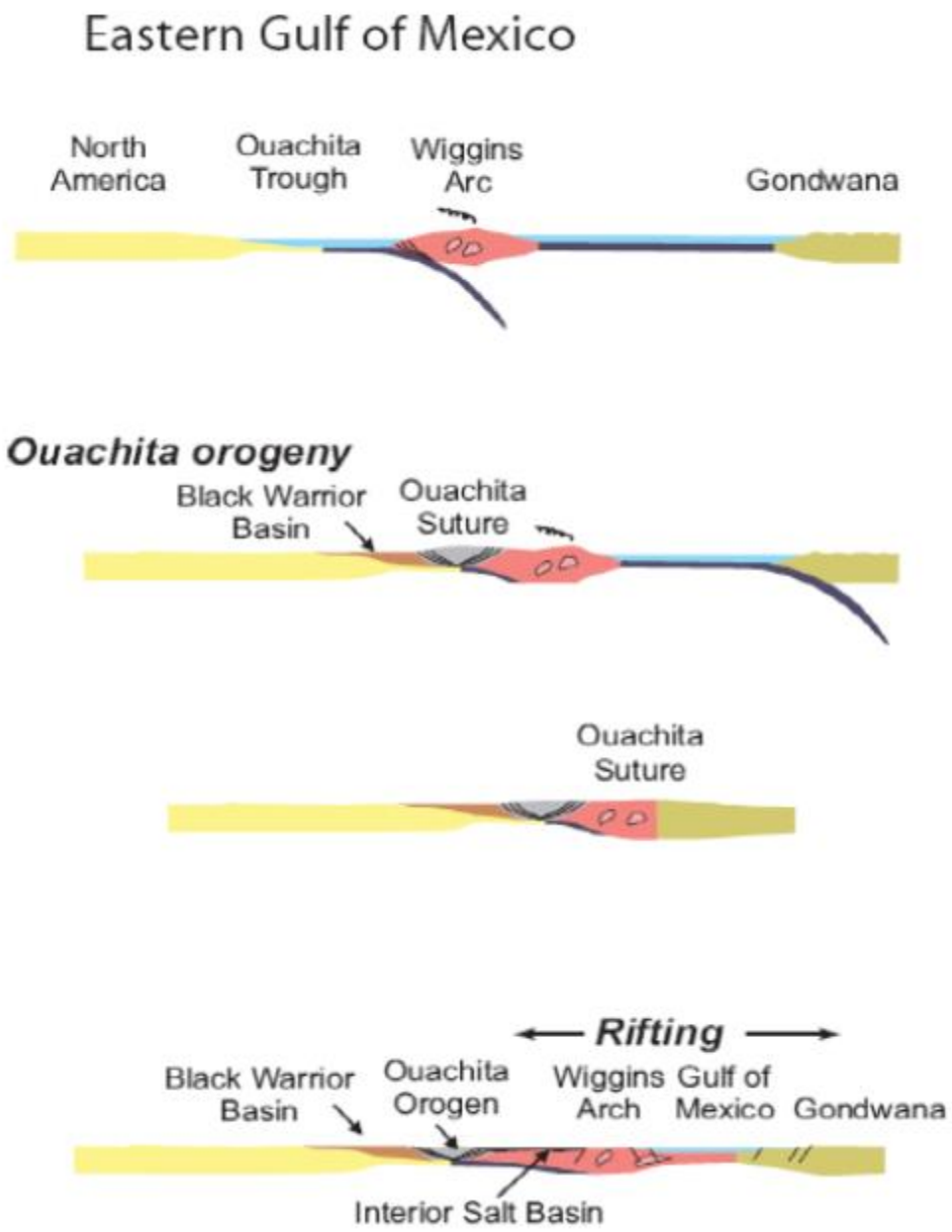

Figure 5. Tectonic evolutions of the Mississippi Gulf of Mexico margin and Ouachita orogeny (Huerta and Harry, 2012)

The Ouachita system is a Paleozoic geosyncline and orogenic belt that borders the southern edge of the North American craton. The fold belt extends more than 2100 km from near the southern terminus of the Appalachians to western Texas, where it passes into Mexico (Figure 6)

(Nicholas and Rozendal, 1975). The Ouachita system was formed during a cycle of opening and closing of Iapetus Sea (Housknecht, 1986), and marks the southern boundary of North American craton (Dickinson, 2009; Raye et al., 2011; Keller, 2012). It is separated from the ancient Mesoproterozoic craton by a transition zone overlaid by the Balcones Igneous Province that also delineated the southern limit of North American craton where the Gulf of Mexico margin terminates abruptly (Figure 7) (Raye et al., 2011; Huerta and Harry, 2012).

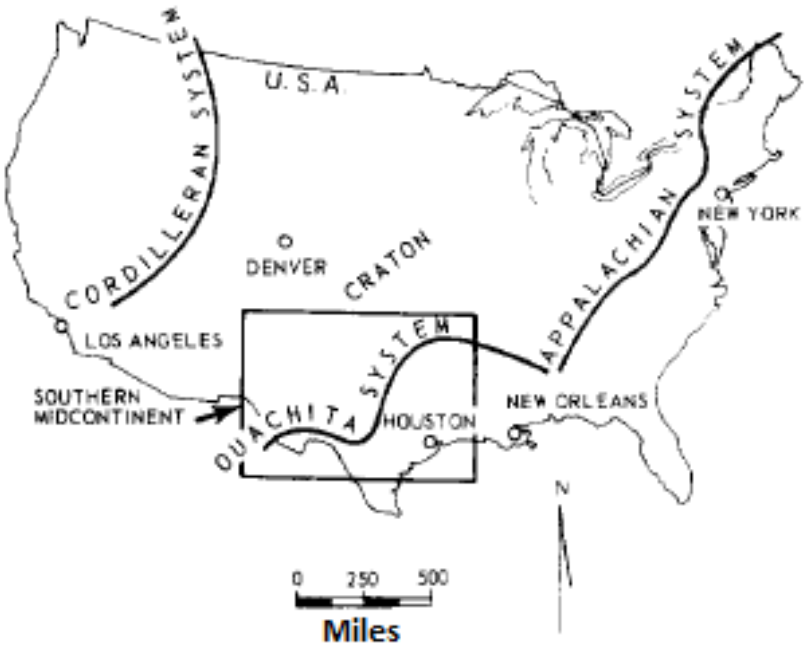

Figure 6. Paleozoic geosynclines of United States and outline of southern Mid-Continent (Nicholas and Rozendal, 1975)

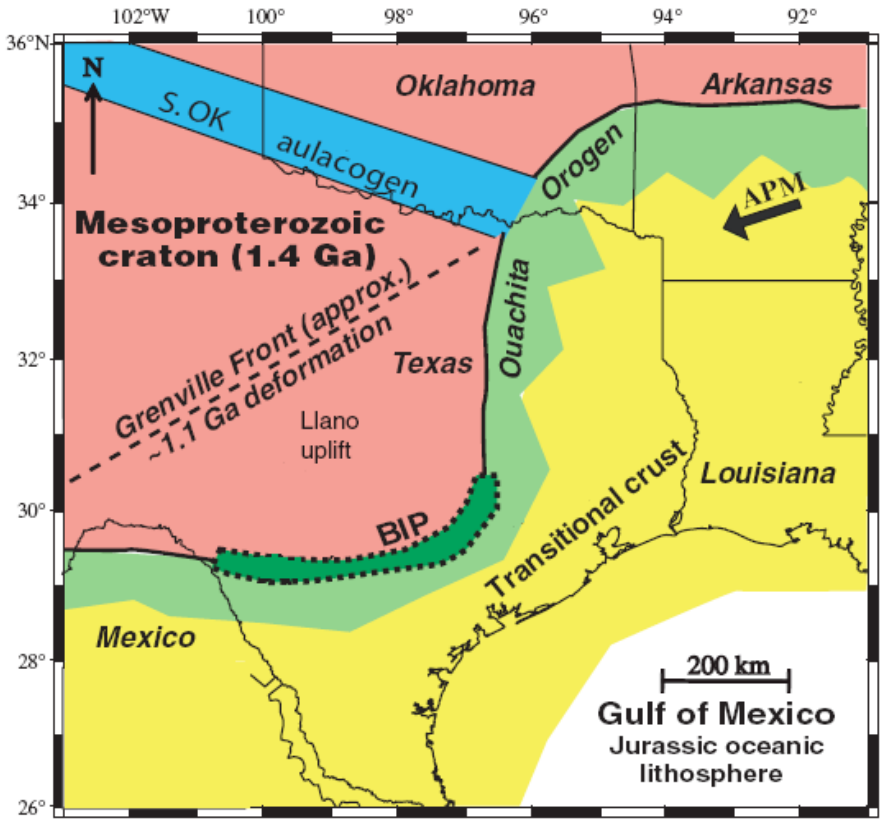

Figure 7. Modern tectonic features of the Texas and Gulf Coast margin. The Balcones Igneous Province BIP is labeled (Raye et al., 2011).

The succeeding continental rifting in Jurassic ~165Ma finally led to the opening of Gulf of Mexico, which defines the present passive continental margin of southeastern Texas (Raye et al., 2011). The extension process thinned the crust beneath the coastal plain that has been subsequently covered with thick sediments that are thickening towards the coastline up to 15km (Figure 8).

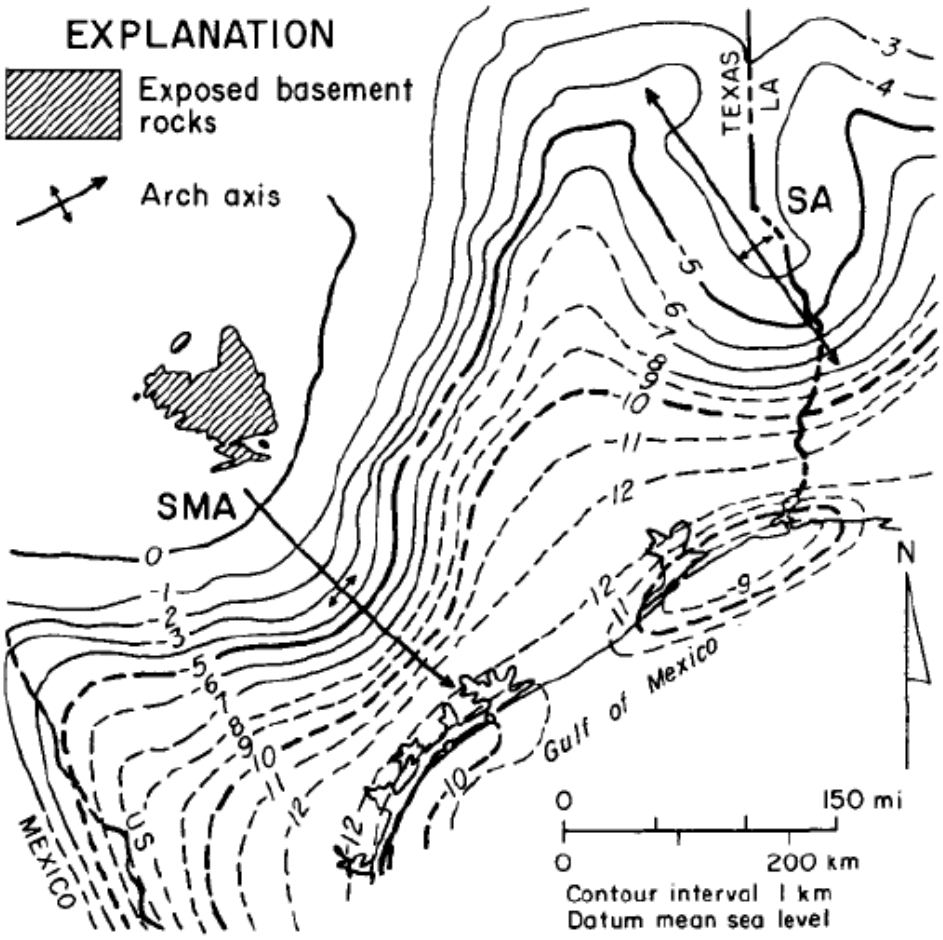

Figure 8. Map showing configuration of basement in northwestern Gulf of Mexico basin based on seismic and well data (Laubach et al., 1990). SA= Sabine Arch, SMA=San Marcos.

2.2 Previous Works

Some previous works have been done for the deep structure in Texas and its vicinity area. Early seismic studies in crustal scale in Texas include seismic reflection, refraction, and surface wave studies in central Texas and in the Gulf Coast region south of the Ouachita system. Refraction and surface wave data (Prewitt, 1969; Stewart, 1968) suggested an average crustal thickness of 53 km of central Texas indicating that the cratonic areas north and northwest of the Ouachita system are typical continental crust based on the thickness and velocity structure. Studies in southeastern Texas established general crustal structures with thinning crust towards the Gulf coastal plain from the northern side of Ouachita system (Cram, 1962; 1970, Keller and Shurbet, 1975). Furthermore, Borehole, seismic and regional gravity data revealed a basement structure dipping to the southeast from San Marcos arches near the Ouachita system, which verified the sedimentary cover thickens toward the Gulf coastal plain (Laubach et al., 1990).

Gravity and aeromagnetic data in Texas and the Gulf of Mexico were processed to produce Bouguer gravity anomaly and magnetic anomaly maps (Figure 9) (Bankey et al., 2002; Mickus, 2009). The most prominent magnetic anomaly is a large-amplitude maximum that parallels the coastline from Mexico to Lafayette, Louisiana (Figure 9B, anomaly 1).

In contrast, the same region on the Bouguer gravity map is characterized by a small-amplitude maximum (Figure 9A, anomaly 2). The high-amplitude magnetic anomaly (Figure 9A, anomaly 1), and it has been interpreted as an indication of a volcanically rifted margin. In addition, a high-amplitude magnetic and a Bouguer gravity anomaly are presented in central Texas associated with the Llano uplift. It is noticeable that a clear boundary exists between the Llano uplift and the Coastal Plain extending to northeast direction, which is highly correlated to the Ouachita Mountain Belt. A presumable cross-section of crust is also approximated in their study, which illustrates strong lateral variation of crustal thickness (Moho depth variation) beneath the southeast Texas (Figure 9C).

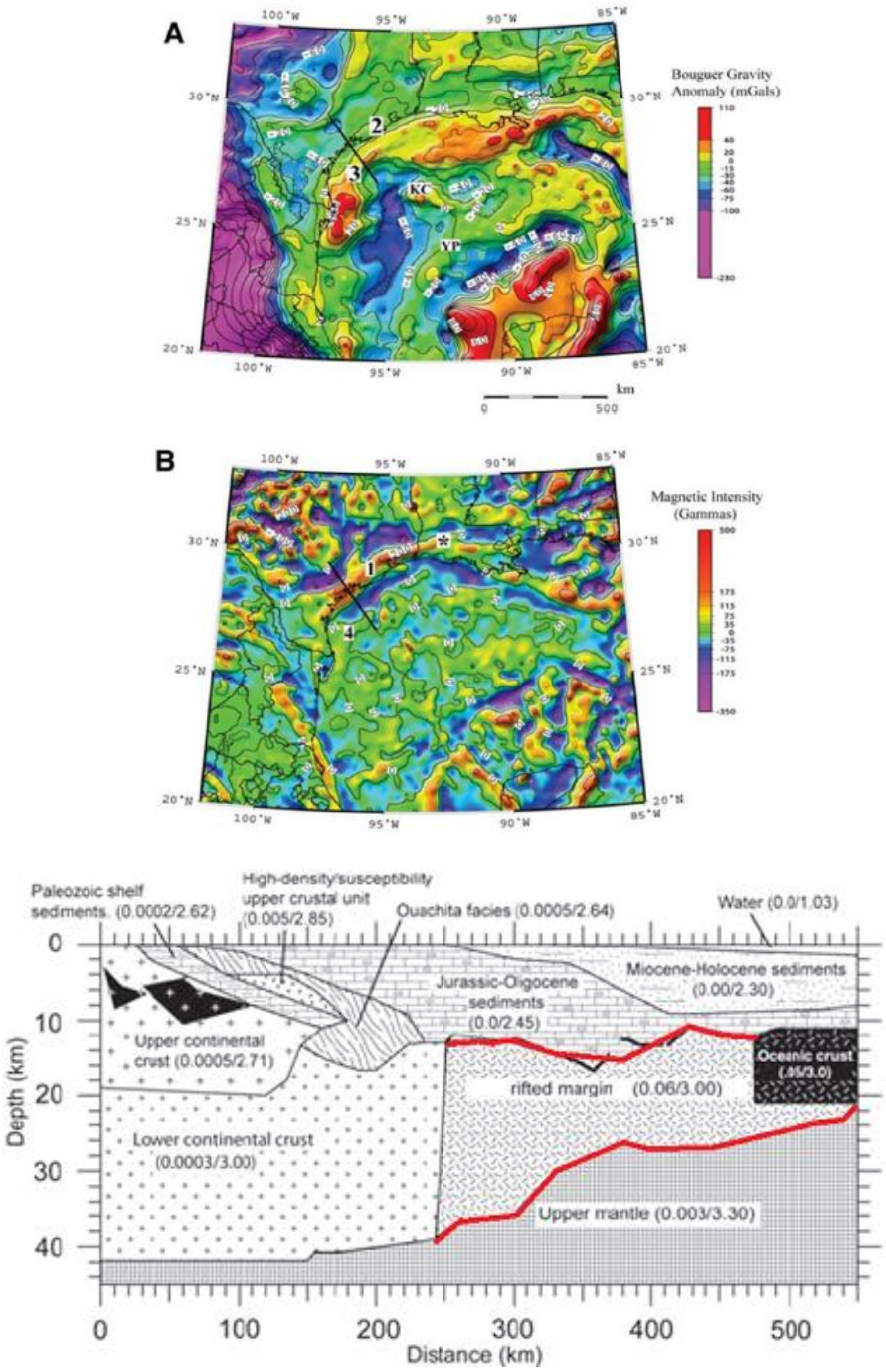

Figure 9. Bouguer gravity anomaly (A) and magnetic intensity map (B) of Texas Coastal Plain and surrounding regions. Contour intervals are 10 mGal and 100 gammas, respectively. Thick line represents location of gravity/magnetic model, where the cross-section of Texas coastal plain (C) is built. The model is defined by a short zone of crustal thinning and extension across the margin (Modified from Mickus et al., 2009)

Rayleigh wave-dispersion experiments carried out by Keller and Shurbet (1975) using different stations in Texas (Corpus Christi, Edinburg, Laredo, San Marcos, and Houston, Figure 10A) show that crustal structure is generally similar along all profiles extending from the Llano Uplift southeastward to the Gulf of Mexico. A generalized crustal structure model proposed by Keller and Shurbet (1975) is shown in Figure 10B. Based on Rayleigh wave-dispersion data, the upper layers with V_p lower than 5.2 km/s are interpreted as Mesozoic and Cenozoic sedimentary rocks, the upper crustal layer V_p above 5.2 km/s is interpreted to consist primarily of Paleozoic metamorphic rocks, and the lower crustal layer with V_p lower than 6.9 km/s may relate to the mafic igneous rocks (Figure 10C). Gravity and refraction data suggest that the crust is thinning towards the Gulf coastal plain where the thick Paleozoic and Mesozoic sediments present.

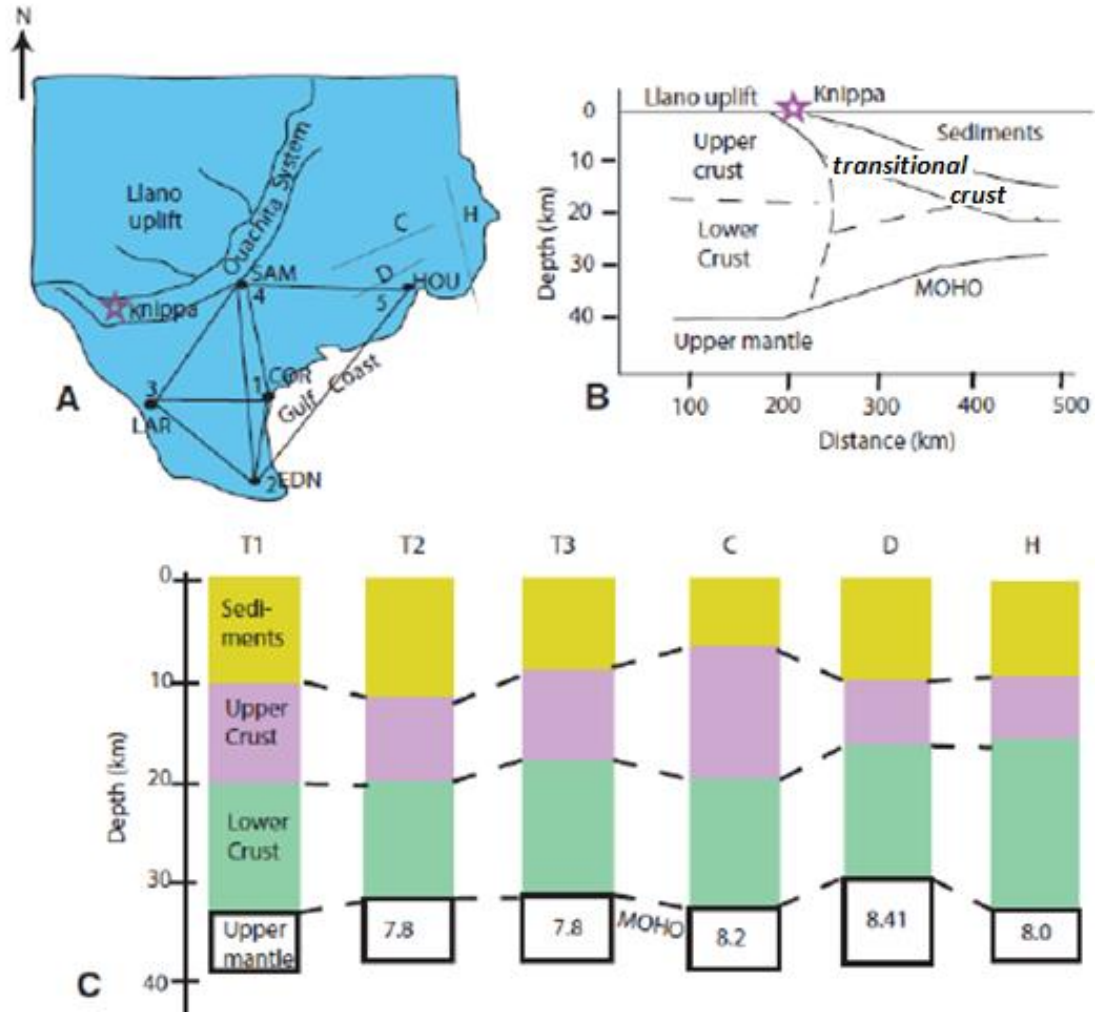

Figure 10. (A) Index map showing Knippa (star), seismograph stations: LAR—Laredo, COR—Corpus Christi, EDN—Edinburg, SAM—San Marcos, HOU—Houston (Keller and Shurbet, 1975), C—Cram (1961, 1962), D—Dorman et al. (1972), H—Hales et al. (1970) refraction line and gravity profiles 1, 2, 3, and 4. T1 (stations 2, 4, and 5), T2 (stations 1, 2, and 3), and T3 (stations 1, 3, and 4) are tripartite locations. (B) Generalized crustal structure model proposed by Keller and Shurbet (1975). (C) Crustal structure as interpreted from seismic velocities. (Raye et al., 2011)

Yao (2013) conducted a research in Texas based on Rayleigh wave tomography from seismic ambient noise. According to his study, phase velocities at periods from 6 s to 40 s show positive anomalies within the Laurentia craton, while the negative anomalies are coincident with the

transitional crust beneath the Texas Gulf coastal plain. The 3-D Shear-wave velocity models of four crustal layers were derived from the inversion of phase velocity (Figure 11). The anomalies are highly correlated with the major geological features of Southeastern Texas. The area with high velocity anomalies corresponds to the Llano uplift and Ouachita zone, and the low velocity anomaly is consistent with the presence of thick sediments within the Gulf coastal plain.

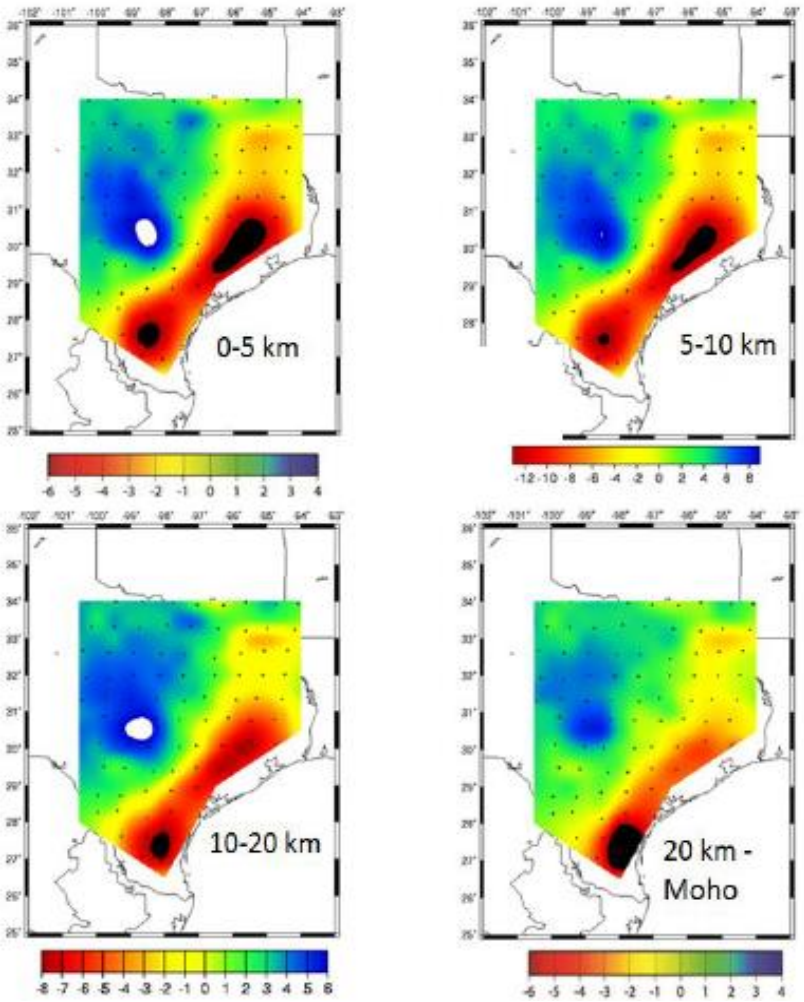

Figure 11. 3-D Shear-wave velocity anomaly maps from crust of East Texas in percentage from Ambient Noise Seismic data (Yao, 2013).

CHAPTHER 3

DATA

The data used in this study were acquired at 66 broadband stations of the Transportable Array network of the USArray. The selected stations cover the Texas coastal plain, the Ouachita orogenic belt, and the Llano uplift tectonic provinces and provide an optimum coverage for mapping the variation of crustal structure in the southeastern-central Texas (Figure 12).

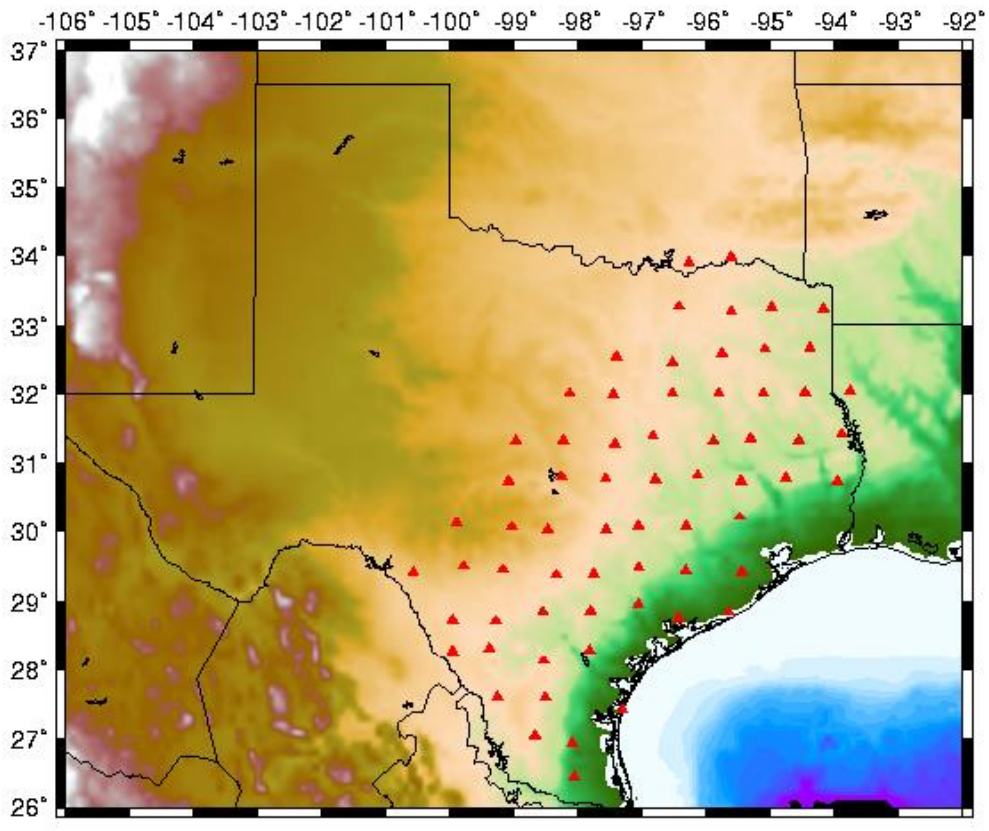

Figure 12. Topography map and station network of southeast Texas consists of selected broadband stations for the P-receiver function study.

The distribution of the stations spans from 26.46 ° N to 33.98 ° N in latitude and 93.89 ° W to 100.58 ° W in longitude. The longest profile extends about 400km in the direction across the coastline strike and 500km along the strike. These stations are operated at varying periods from 2009 up to present.

Two criteria are applied in selecting earthquake events that occurred during the station operation time and can be used to compute P-receivers. 1) Epicentral distances of the events are between 30-95 °. Events with distance less than 30 ° will not be able to satisfy the general requirement of nearly vertical P wave ray path for P receiver function calculation. For events with distance over 95 °, a P wave propagates through the core-mantle-boundary and its amplitude is largely reduced due to energy partitioning at the boundary. 2) Magnitudes of the selected events are larger than 5.5 Mb to ensure high signal/noise ratio.

According to the above criteria, a total number of 257 earthquake events recorded at 66 stations have been selected. The distribution of earthquakes is shown in Figure 13. These earthquakes mainly come from three groups of back azimuth, which are NW, SSE and WSW. Most of the events have magnitudes above 5.9 that provide data with high signal-to-noise ratio. Three-component seismograms for the selected

events were obtained through the IRIS Data Management Center (www.iris.edu) using the BREQ_FAST data-request tool.

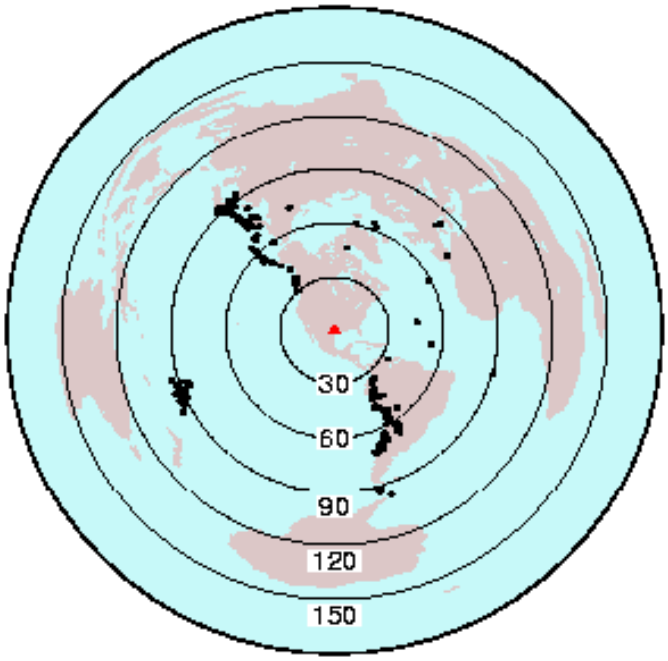

Figure 13. Epicenter distribution of earthquakes used in the P-receiver function study. Red triangle is the center of selected TA stations (southern Texas). Black dots represent epicenters of the earthquakes. Concentric circles indicate distances (degree) from the center of the group of TA stations.

However, although a large number of events were selected, seismograms recorded at stations in the Texas coastal plain is severely contaminated by noises generated within the thick sedimentary layers. After pre-processing the data and removing noisy events and stations, 116 events at 47 stations yielded useful data for P-receiver function analysis.

CHAPTER 4

METHOD

The receiver function method is a commonly used technique to study the earth's structure. It is based on P and S-wave observations from teleseismic events recorded by three-component broad-band seismic stations (Langston, 1977). The resulting receiver function is obtained by removing the effects of source and mantle path from raw seismograms to reflect responses to the structure beneath the receiver (Langston, 1977; Owens et al., 1984; Mohsen, 2004; Sodoudi, 2005). The receiver-function method has already been applied successfully to image the lateral variability of major velocity boundaries in the crust and upper mantle (Langston, 1977; Owens et al., 1984).

Generally, the impinging P wave generated from teleseismic events will be converted to S wave (Ps) and other multiples (PpPs, PsPs+PpSs) at interfaces associated with large seismic velocity contrast such as the Moho, the discontinuity between the upper mantle and lower crust. A typical receiver function including the P to S conversion and multiples from the Moho is shown in Figure 14 (Ammon, 1997; Sodoudi, 2005). The amplitude, arrival time, and polarity of the locally generated Ps phases largely rely on the S-velocity structure beneath the recording

station (Ammon, 1997).

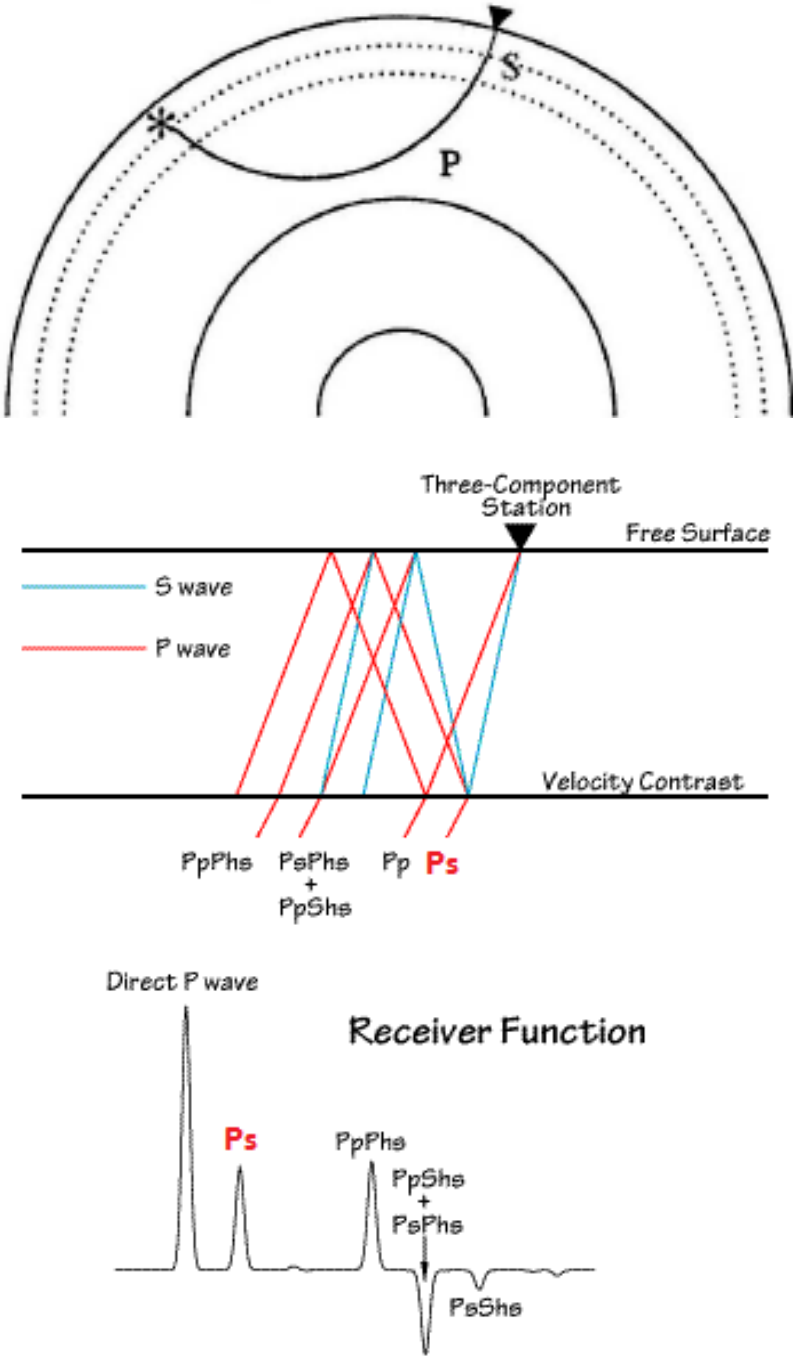

Figure 14. Ray paths of teleseismic waves and P-receiver function (Modified from Ammon, 1997; Geissler et al., 2000)

4.1 Individual Receiver Function Calculation

The standard procedure of P-receiver function construction involves filtering 3-component seismograms, rotating the ZNE (vertical-north-east) components into the ZRT (vertical-radial-transverse) components, and deconvolving the R and T components with the Z component. These steps are described in detail below.

4.1.1 Filtering and Rotating Seismograms

In order to extract desired signals, a band-pass filter with corner frequencies 0.05 and 1Hz is applied to remove unwanted noise from the teleseismic body wave. A time window of 120s used for windowing the seismograms. An example of raw data and processed waveforms after filtering is shown below (Figure 15):

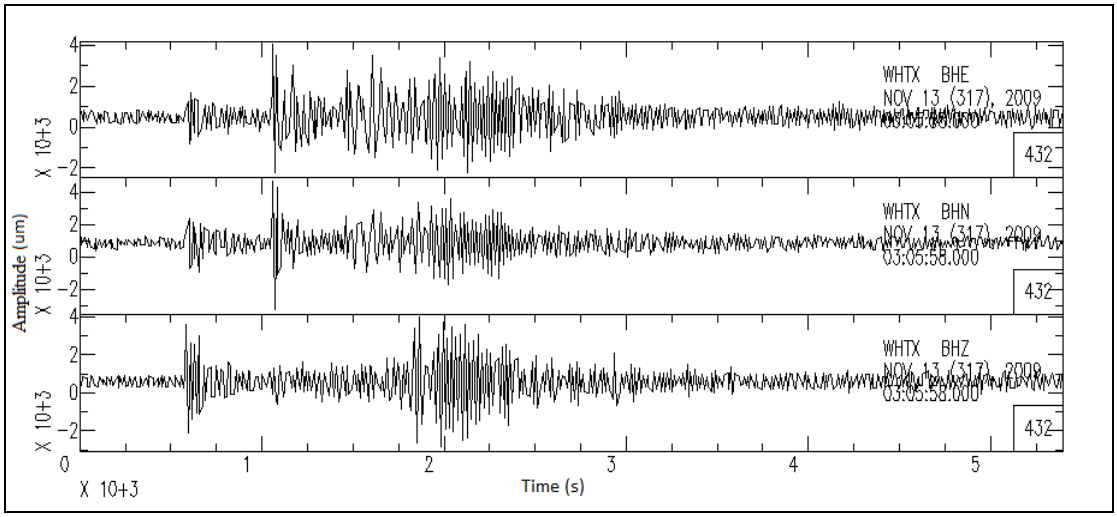

(a)

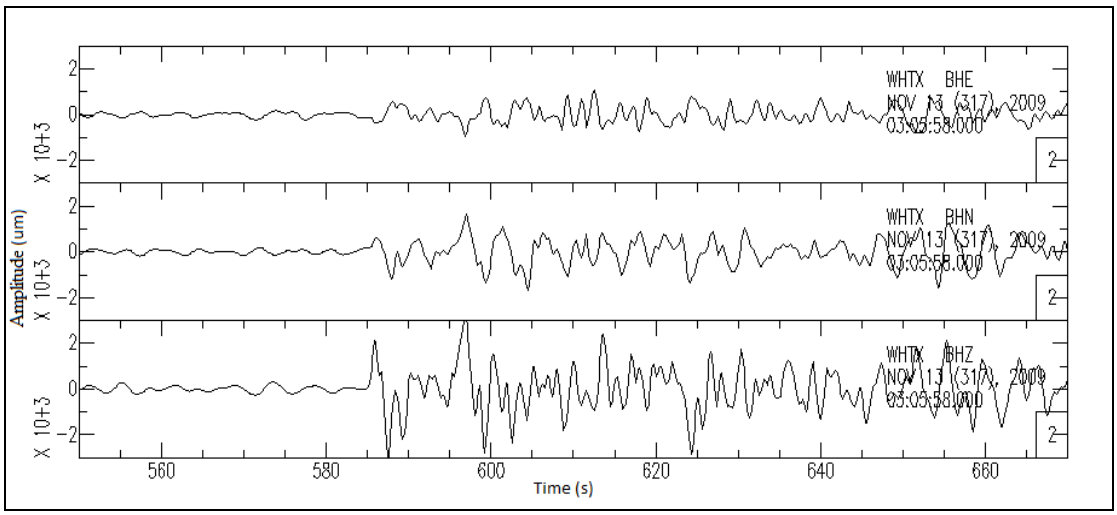

(b)

Figure 15. (a) The original 3 components seismograms of event 2009-11-13 at station WHTX. (b) The filtered and window-cut 3 components seismograms of event 2009-11-13 at station WHTX.

The windowed and filtered seismograms are rotated from the ZNE coordinate into the ZRT coordinate system, where the vertical component Z is dominated by P wave energy, R is the radial component that mainly contains SV energy, and T is the transverse component containing SH energy (Figure 16). For horizontally layered homogeneous media, the

converted S wave energy is exclusively contained on R component, while T component gives additional information of heterogeneous or anisotropic structures (Sodoudi, 2005). For isotropic media, energy on T component can reflect dipping interfaces that also give distinctive signatures on R component (Owen and Crosson, 1988). This study will concentrate on the features of major structure by analyzing radial component.

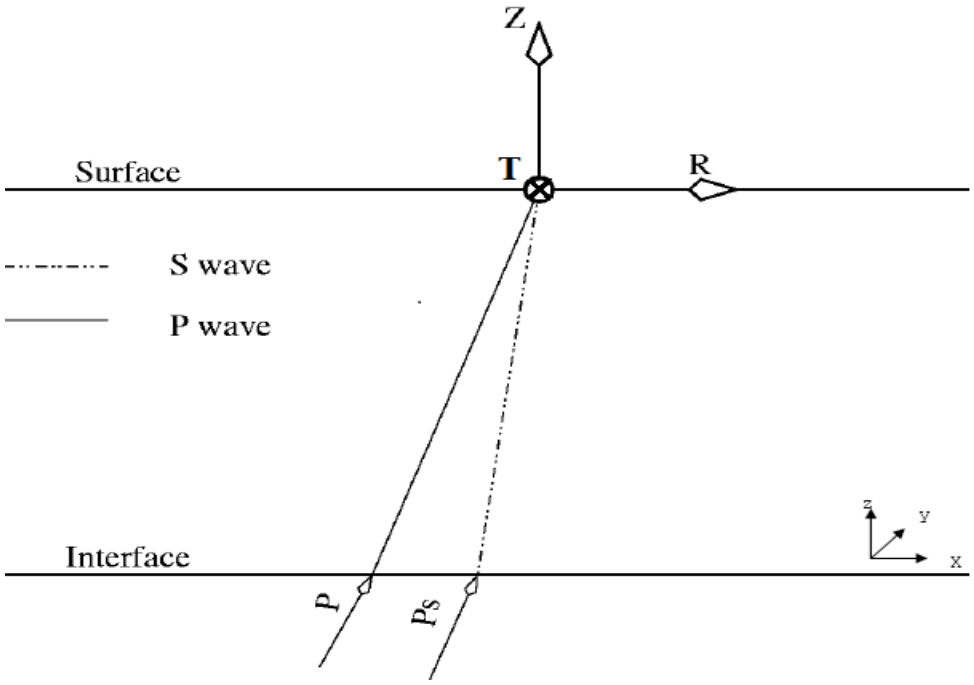

Figure 16. Seismogram is converted from vertical, NS, EW components to ZRT component (modified from Mohsen, 2004)

4.1.2 Deconvolution

To isolate individual receiver function and remove the effects of the source and ray path, a source equalization method is carried out by

deconvolving the R and T component seismograms with the signal on the vertical component (Langston, 1979; Owens et al., 1984). According to the equalization theory of Langston (1979), the three-component displacement responses in time domain of a P plane wave at a station can be represented by:

$$D_V(t) = I(t) * S(t) * E_V(t)$$

$$D_R(t) = I(t) * S(t) * E_R(t)$$

$$D_T(t) = I(t) * S(t) * E_T(t)$$

where $D_V(t)$, $D_R(t)$ and $D_T(t)$ are the vertical, radial and transverse components of the teleseismic body wave, respectively; $I(t)$ is the instrument response and $S(t)$ is the source time function; $E_V(t), E_R(t)$ and $E_T(t)$ are the near-station structure responses on vertical, radial and transverse components; the asterisks represent the convolution operator. Theoretically, the vertical component of ground motion for a steeply incident P wave consists of a large direct arrival followed by only minor arrivals of crustal reverberations and phase conversions (Langston, 1979; Owens et al., 1984). Therefore the vertical component of structure response can be approximated as a pulse-like Dirac function, i.e., $E_V(t) \approx \delta(t)$, which makes the vertical component:

$$D_V(t) \approx I(t) * S(t)$$

On the other hand, Ps conversions have much stronger amplitude on the two horizontal components than the vertical one. Thus, the expected

waveforms can be extracted from the horizontal components as radial and transverse receiver functions $E_R(t)$ and $E_T(t)$. The process is given by:

$$E_R(\omega) = \frac{D_R(\omega)}{D_V(\omega)} = \frac{D_R(\omega) \cdot D_V^*(\omega)}{\Phi_{SS}(\omega)} \cdot G(\omega)$$

$$E_T(\omega) = \frac{D_T(\omega)}{D_V(\omega)} = \frac{D_T(\omega) \cdot D_V^*(\omega)}{\Phi_{SS}(\omega)} \cdot G(\omega)$$

In these expressions, $G(\omega) = e^{-\omega^2/4\alpha^2}$ is the transform of Gaussian which is used to limit the final frequency band, where α defines the band width by excluding the high-frequency signals from the original recordings. $\Phi_{SS}(\omega) = \max\{D_v(\omega)D_V^*(\omega), c\max[D_V(\omega)D_V^*(\omega)]\}$, where c is the water level coefficient controlling the minimum allowable spectral amplitude of the vertical component; $D_V^*(\omega)$ is the complex conjugate of $D_V(\omega)$. In this study, the water level c is set to 0.01 and the Gaussian scale α is chosen to be 0.7. Then, $E_R(w)$ and $E_T(w)$ are Fourier transformed back to time domain. The resulting radial component seismograms $E_R(t)$ are the desired P receiver functions. It mainly consists of the primary P-to-S converted energy and multiples from crustal and mantle discontinuities beneath seismic stations. Positive amplitudes in the receiver function indicate a velocity increase with depth, while negative amplitudes correspond to a velocity decrease with depth. An example also shows the isolated P-receiver function after rotation and deconvolution (Figure 17):

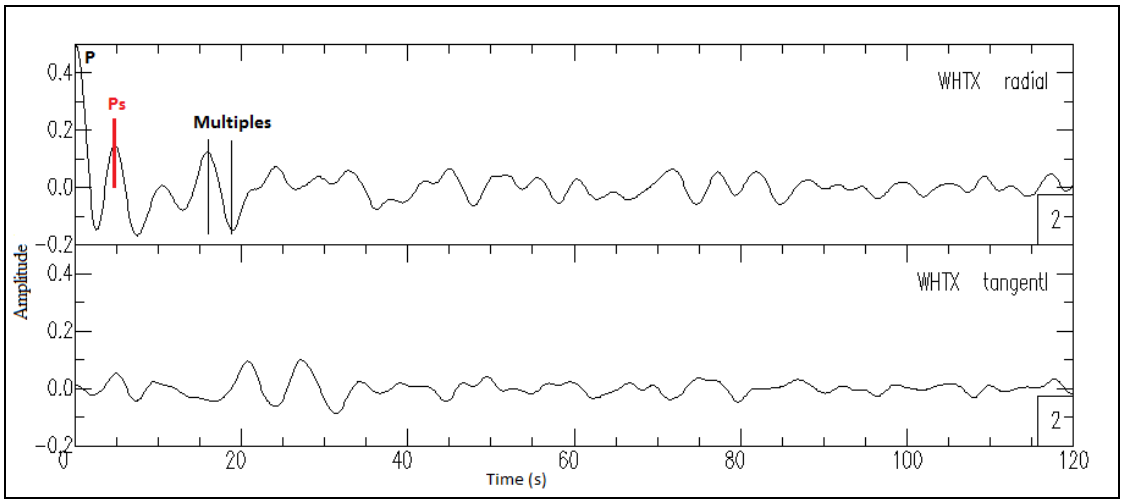

Figure 17. The isolated radial and tangential components of original seismogram at station WHTX: P waveform is deconvolved from all three components. Then the radial component is called P receiver function. The P onset is shifted to zero time. The first converted Ps phase at ~5s represents the conversion from Moho discontinuity, while the multiples arrive at 15-19s delay time.

4.2 Move-out Correction and CCP Stacking

In order to increase the coherent signal energy and suppress noise, receiver functions can be stacked depending on their ray paths (Zhu, 2000). However, time variations associated with different epicenter distance (source-receiver separations) may compromise the spatial resolution and deliver false structure. Therefore the arrival time of Ps conversion phase on individual receiver function is corrected for vertical incidence and equalized regarding their ray parameters.

A common assumption of receiver function analysis is a planar incoming wave front in a single layer half-space, where the travel time difference of P and Ps wave can be easily calculated (Sodoudi, 2005) (Figure 18). The delay time of Ps conversion phase relative to P wave can be approximated as:

$$\Delta T_{ps}(p; z, V_s, V_p) = T_s + T_h - T_p$$

Where, T_s, T_h, and T_p are traveltimes indicated in Figure 18, p is the ray parameter, z is the depth to the interface, V_s and V_p are the S and P wave velocity in the layer, respectively.

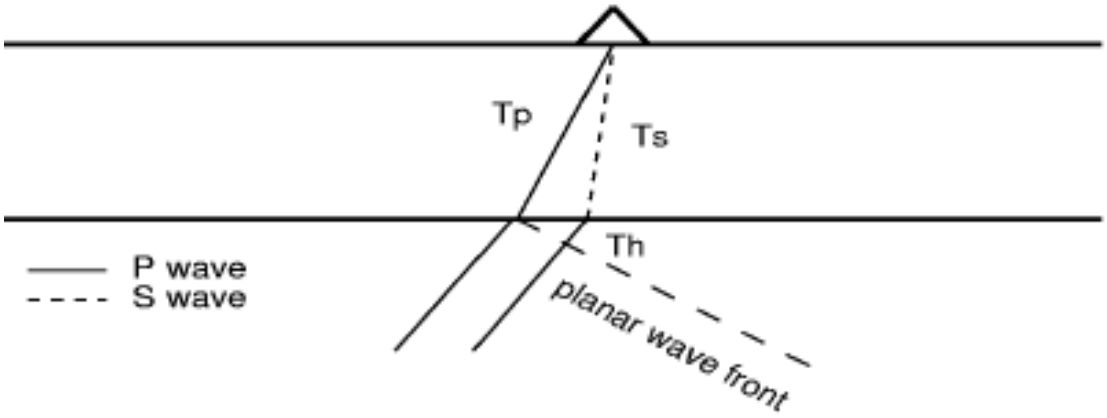

Figure 18. Ray paths of Ps conversion wave relative to the P wave for a layer over a half-space. T_p and T_s mark the traveltime of P and Ps wave with the same ray parameter, respectively. Th is traveltime difference in the half-space for the two rays (Sodoudi, 2005).

Assuming the same ray parameter for P and Ps conversion at the time of incidence, the moveout for Ps conversion is calculated as below, in terms of p, z , V_s and V_p:

$$\Delta T_{ps}(p;z,V_s,V_p) = z(\sqrt{V_s^{-2} - p^2} - \sqrt{V_p^{-2} - p^2})$$

Then, the moveout correction is conducted to adjusted the delay times of Ps conversions of all receiver functions with respect to a reference time, which is the delay time between P and Ps at vertical incidence, where p=0, i.e., $\Delta T_{ps0} = \Delta T_{ps}(0;z,V_s,V_p)$. The magnitude of moveout correction varies with both conversion depth and the ray parameter of impinging P wave (Mohsen, 2004).

Similarly, the moveout curves for the following crustal reverberations, such as PpPs and PsSs, can be expressed in the same format. In addition,

the different shapes of the moveout curves make it possible to distinguish reverberations from primary conversions (Sodoudi, 2005):

$$\Delta T_{PpPs}(p;z,V_s,V_p) = z(\sqrt{V_s^{-2} - p^2} + \sqrt{V_p^{-2} - p^2})$$

$$\Delta T_{PsSs}(p;z,V_s,V_p) = z(3\sqrt{V_s^{-2} - p^2} + \sqrt{V_p^{-2} - p^2})$$

After moveouts are calculated, the common-conversion point (CCP) stacking is applied to receiver functions at single station to illustrate the Moho conversion and further enhance signal-to-noise ratio. In this study, only Ps conversion phase is corrected for moveout based on a global velocity model (IASP91) and stacked to image the structure of the Moho discontinuity. The peak arrival of the Ps conversion on the stacked receiver function can be mapped to depth beneath each station to obtain the Moho depth variation.

4.3 The H-κ Stacking Method

The delay times of Ps converted phases and following multiples in receiver functions can be directly used to estimate average crustal thickness and V_p/V_s ratio by using the H-κ stacking method of Zhu and Kanamori (2000) based on the relation:

$$H = \frac{t_{Ps}}{\sqrt{\frac{1}{V_s^2} - p^2} - \sqrt{\frac{1}{V_p^2} - p^2}}$$

Where H is the crustal thickness, t_{ps} is the travel-time difference of S and P wave in the crust and p is the ray parameter of incident wave. Since the crustal thickness is more dependent on V_p/V_s ratio than V_p or V_s alone, the stacking is conducted in the H-κ domain (Zhu and Kanamori, 2000). The algorithm sums the amplitudes of receiver functions at the predicted arrival time of Moho conversion Ps and its multiples (PpPs, PpSs+PsPs) for various crustal thicknesses H and V_p/V_s ratios (κ) (Figure 19). Then it performs a grid search through the H and κ space to locate the largest amplitudes at the predicted times of different phases, by a given average crustal P velocity.

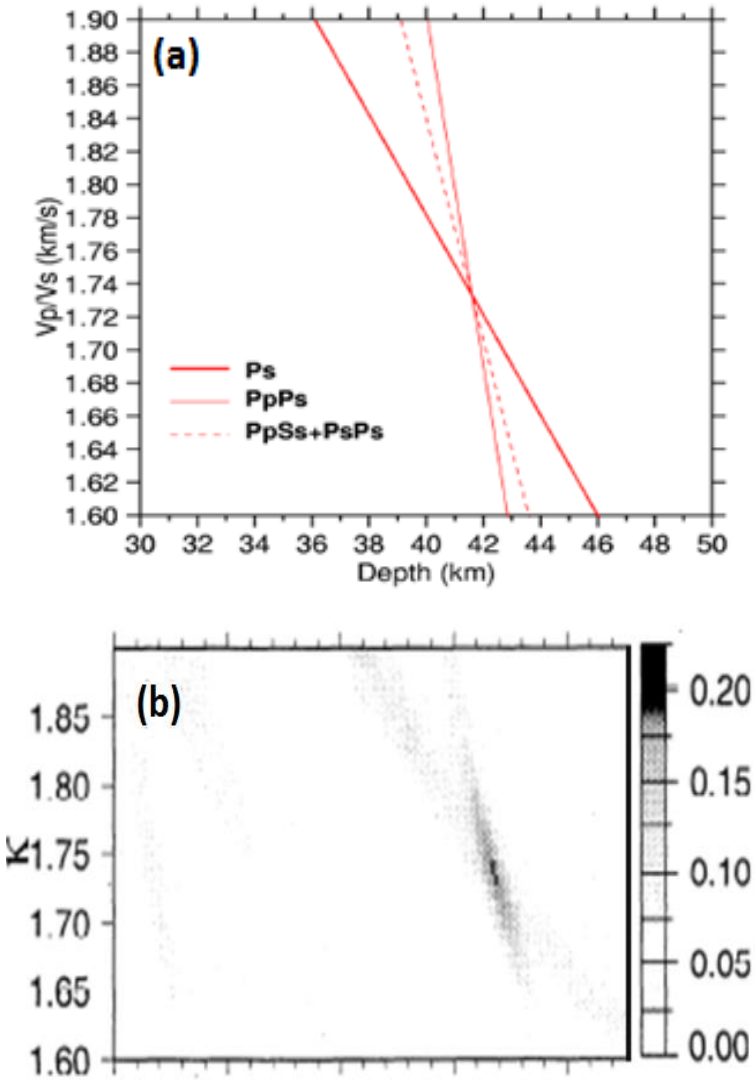

Figure 19. Contributions of Ps and its multiples to the stacked amplitude with respect to H and κ (Zhu and Kanamori, 2000; Sodoudi, 2005).

Concerning the higher signal-to-noise ratio of the primary converted phase (Ps) in comparison to its multiples, amplitudes of different phases are weighted and stacked as following:

$$s(H,\kappa) = w_1 r(t_1) + w_2 r(t_2) - w_3 r(t_3)$$

where $r(t_i)$ are the receiver function amplitudes, t_1, t_2, t_3 are the predicted travel times for Ps, PpPs and PpSs+PsPs corresponding to certain values

of H and κ, w_i is the weighting factor for each phase, and $\sum w_i=1$. Usually the highest weighting factor is associated with the direct conversion ($w_1>w_2+w_3$), while the crustal multiples have similar slopes (Figure 19). The function s(H, κ) reaches a maximum when all three phases are stacked coherently with the optimum values of crustal thickness and V_p/V_s ratio.

The H-κ method simultaneously stacks large amounts of teleseismic receiver functions from different distances and directions, which suppresses the effects of lateral structure variation and produces an average crustal model beneath the stations.

CHAPTHER 5

RESULTS

In this chapter, the results obtained from teleseismic P receiver function analysis are presented and explained. The data processing procedure is briefly summarized below. First, P-receiver functions are computed for all data following the steps described in chapter 4. Second, the individual receiver functions for each station are corrected for moveout based on the global velocity model IASP91 and stacked to form a single trace. Third, the time of the Ps phase from the Moho on all stacked receiver functions are estimated and migrated to depth using the reference vertical ray path. Furthermore, the H-κ stacking method is applied to simultaneously determine the crustal thickness and V_p/V_s ratio beneath each station. The Moho depths beneath each station are also used to generate maps by interpolation. The results determined from the CCP and H-κ stacking methods are compared and incorporated to evaluate the crustal structure.

5.1 Results from CCP Stacking

5.1.1 Observed P-Receiver Functions

CCP stacking is applied at all 66 stations, Only 35 of the 66 stacked receiver functions show clear P to S conversion from the Moho and are finally used for constructing the map of Moho depth variation. Figures 20-24 show P receiver functions at eight stations that are located at different places of the study area.

The aligned P-receiver functions are sorted with increasing back azimuth. The sum traces in the upper panels represent the stacked P receiver function for each station. The waveforms are plotted in a time window of 0 to 30 seconds, where direct P arrivals are fixed at zero time. Results from station 433A and 533A which are located in the Llano uplift area, are shown in Figure 20. P-receiver functions at these two stations exhibit clear primary Ps conversion from the Moho discontinuity with a delay time of about 5 s while reverberations generated between the surface and the Moho can also be observed at 10 to 20 s on some receiver functions. Figure 21 shows stations 135A and WHTX located in the northern portion of the Ouachita zone of Texas. The observed receiver functions at these two stations demonstrate the similar features as stations shown in Figure 20, which exhibit high signal-to-noise ratio with clear Ps

conversion phases at ~ 5s, designating the Moho discontinuity beneath the corresponding stations.

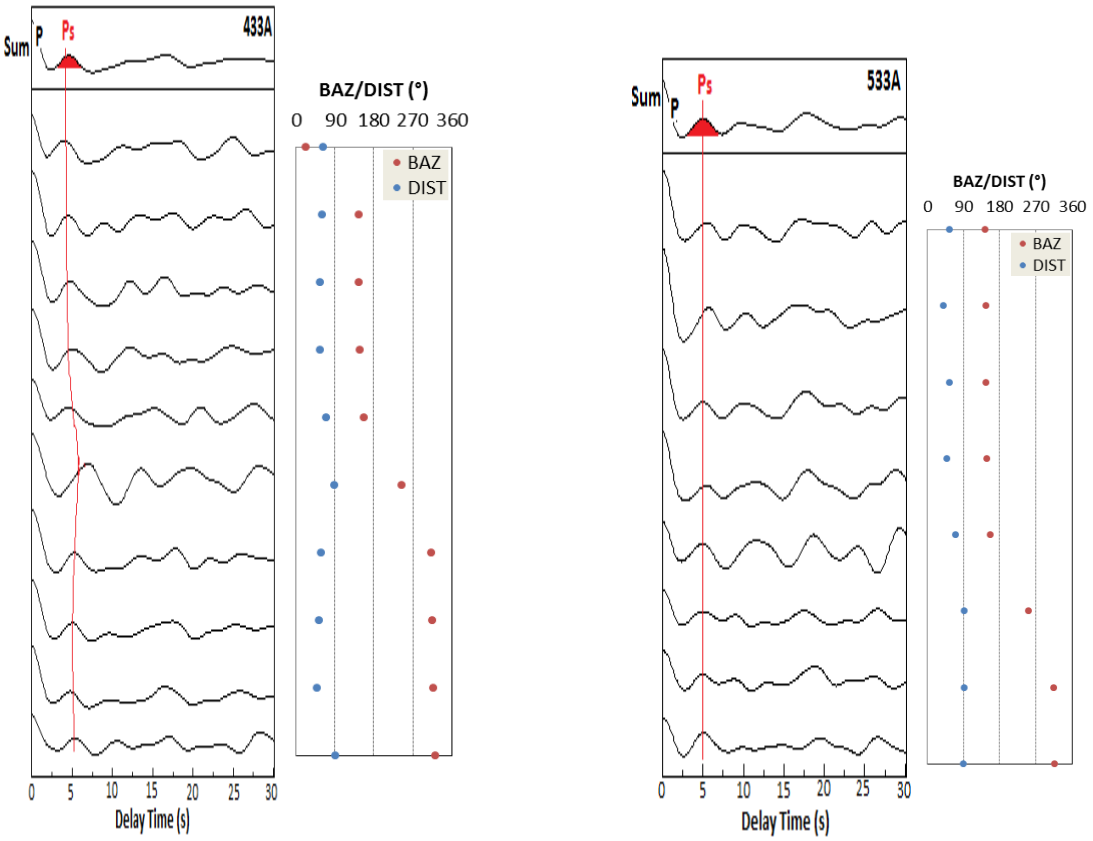

(a) **(b)**

Figure 20. Individual and stacked P-receiver functions obtained at stations 433A (a) and 533A (b) located at the Llano Uplift area of central Texas. The individual ones are sort by increasing back azimuth. The P onsets are fixed at time zero, and Ps conversions are clearly located (marked by red).

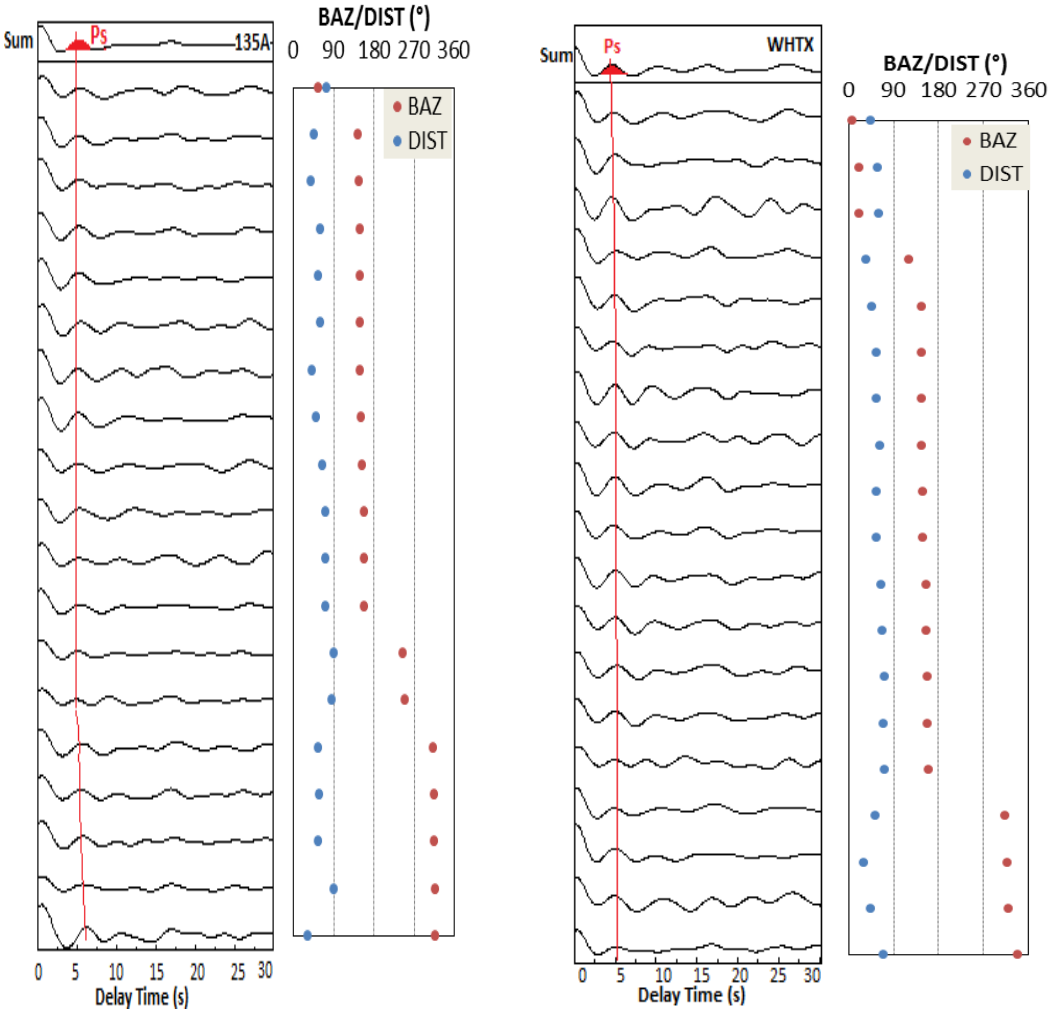

(a) **(b)**

Figure 21. Individual and stacked P-receiver functions calculated at stations 135A (a) and WHTX (b) located in the Ouachita zone of Texas. The individual ones are sort by increasing back azimuth. The P onsets are fixed at time zero, and Ps conversions are clearly located (marked by red) (For WHTX, 48 individual receiver functions are originally selected for stacking, but only 19 of them are presented to deliver a clear shape of the waveforms).

Figure 22 shows results at stations 336A and 832A, which are located on the northeastern and southeastern side of Ouachita belt, respectively. The receiver functions are displaying slightly different features from those described before. The Ps conversion phase of receiver functions at these stations can be recognized at about 4 s, suggesting a shallower Moho

compared with that of the Ouachita and Llano uplift zone. The abrupt thinning of crust (decrease of delay time) may mark the transition from the Ouachita orogenic and Mesoproterzoic crust to the extended crust beneath the Texas coastal plain.

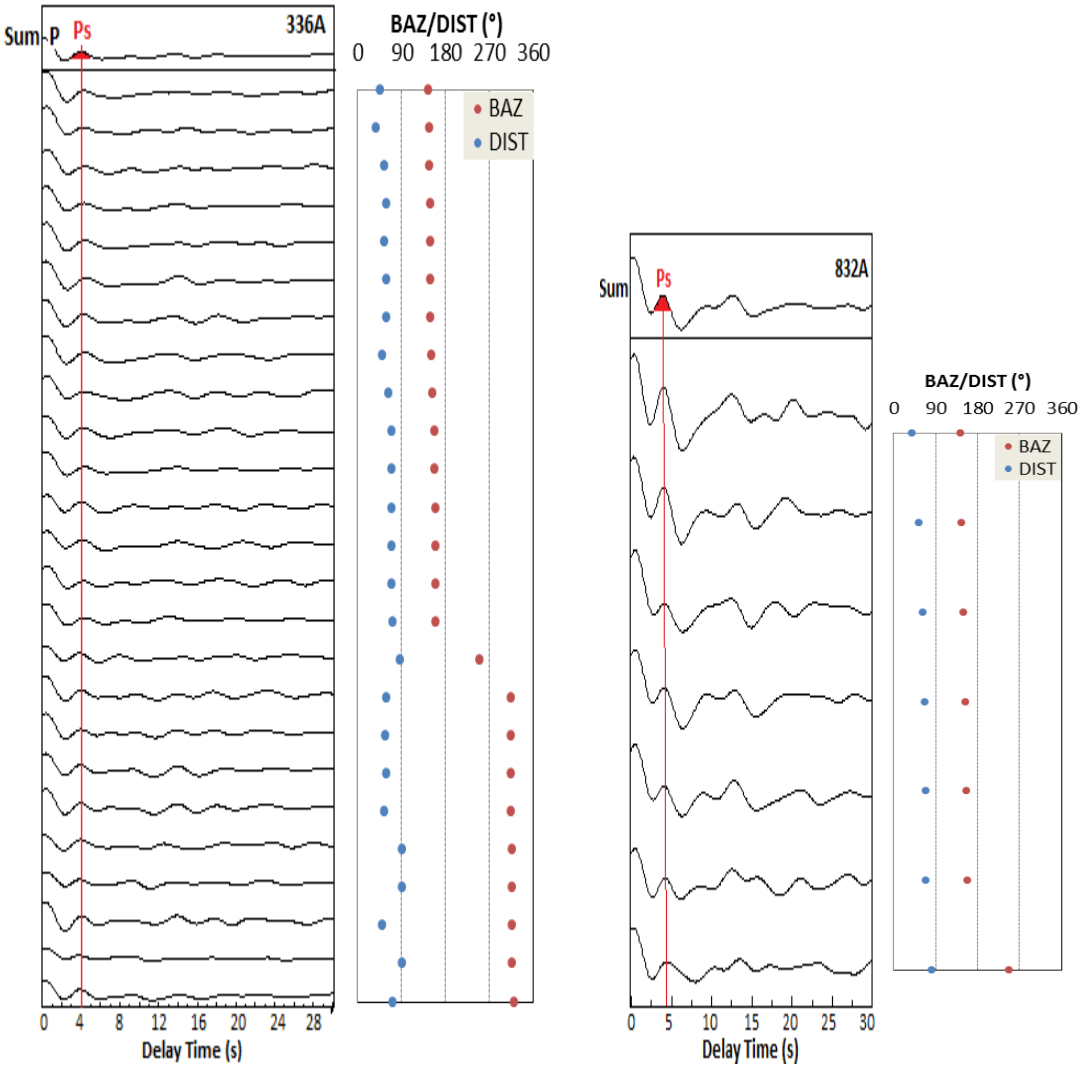

(a) **(b)**

Figure 22. Individual and stacked P-receiver functions calculated at stations 336A (a) and 832A (b) located on the northeastern and southern side of Ouachita belt, respectively. The individual ones are sort by increasing back azimuth. The P onsets are fixed at time zero, and Ps conversions are clearly located (marked by red).

Moreover, there are several stations exhibit anomalies by comparing with the surrounding ones. For example, the Ps conversion from Moho appears at a delay time around 6.2 s at the stacked receiver function of station 632A, which corresponds to the Moho depth over 55 km (Figure 23). This estimation doesn't conform to the regional geology according to the previous study in this area.

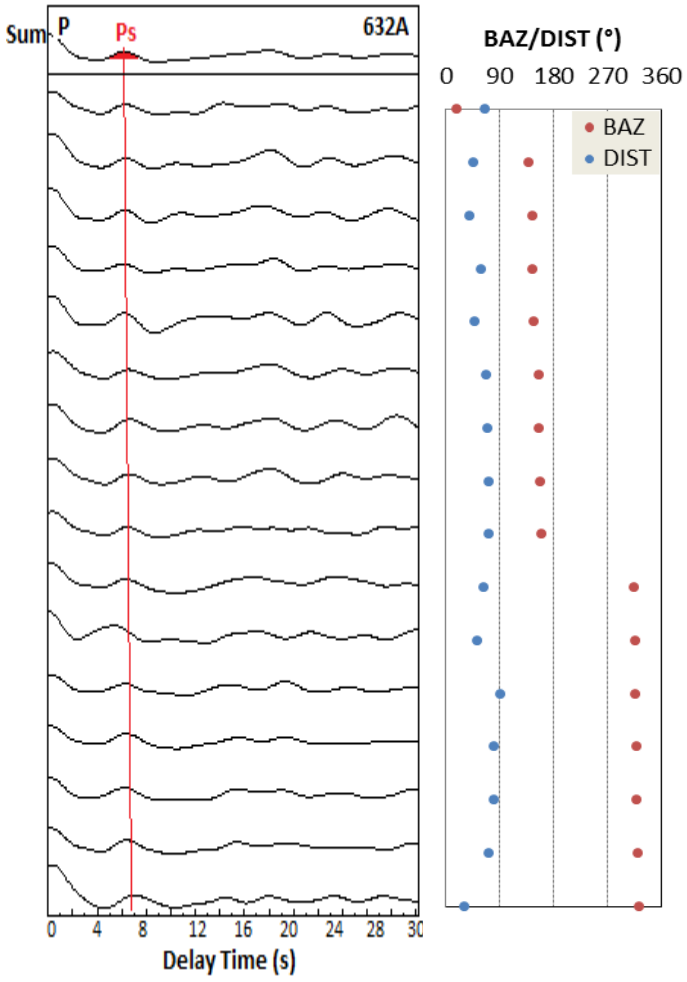

Figure 23. Individual and stacked P-receiver functions calculated at stations 632A located at and southeastern edge of Ouachita belt. The individual ones are sort by increasing back azimuth. The P onsets are fixed at time zero, and Ps conversions are clearly located (marked by red).

Unfortunately, most of the stations approaching the Gulf coastal plain and the coast rifted margin did not yield good receiver functions with clear Ps conversion phase from the Moho discontinuity. Example of such receiver functions from 035Z is shown in Figure 24. In spite of the absence of clear Ps conversion from the Moho at stations near the coast, the receiver functions provide information from the crystalline basement underlying the sediments. As seen from the figure above, the first arrivals marked by the black line with the largest amplitude show a phase shift about 1- 4 s, which are probably the Ps conversions generated from the basement of the sedimentary layer. It is noticeable that the delay time of basement Ps phase varies with their azimuths, suggesting a dipping structure of the interface.

Assuming reasonable velocity of the shallow sedimentary layers, the delay time of the basement Ps conversion can be used to estimate the thickness of sediments beneath each station. The phase appears right after the basement Ps conversion seems to be the Ps conversion from Moho. However, it is interfered with other multiples from the shallow interfaces and is not reliable in imaging the Moho depth.

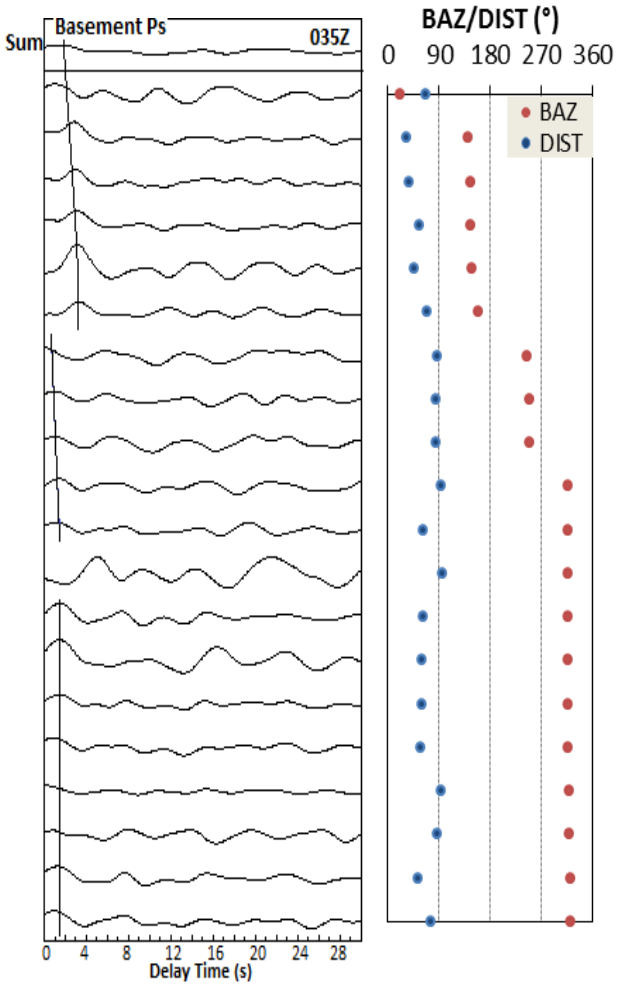

Figure 24. Individual and stacked P-receiver functions calculated at stations 035Z located in the very southern corner of Texas. The individual ones are sort by increasing back azimuth. The Ps conversions of basement at large back azimuth above 300 are marked by blue line, while the smaller ones are marked by black.

5.1.2 Profile of Stacked P-Receiver Functions

A SE-NW profile of stacked receiver functions is presented in Figure 25. The profile is located in northeastern Texas and nearly perpendicular to the coastline across the coastal plain and the Ouachita belt. Stacked receiver functions at stations along the profile displays a dipping Moho with crust thickening towards the northwest for the NW part (marked by

red line). Nevertheless, receiver functions at stations 437A, 538A and 638A, which are located in the eastern Texas sedimentary basin, do not convey a clear conversion phase that can be associated with a valid Moho depth. The phases marked by red circles at the three stations are too late to be the P to S conversion from the Moho, which re probably multiples from the base of the sediments. The phases with a delay time of ~1 to 3 s appear at the southern SE stations, which are marked by the green line, are probably the converted phase from the interface between sediments and crystalline basement. The delay time of this phase slightly increase towards the coastline from 437A to 638A, indicating seaward thickening of sediments.

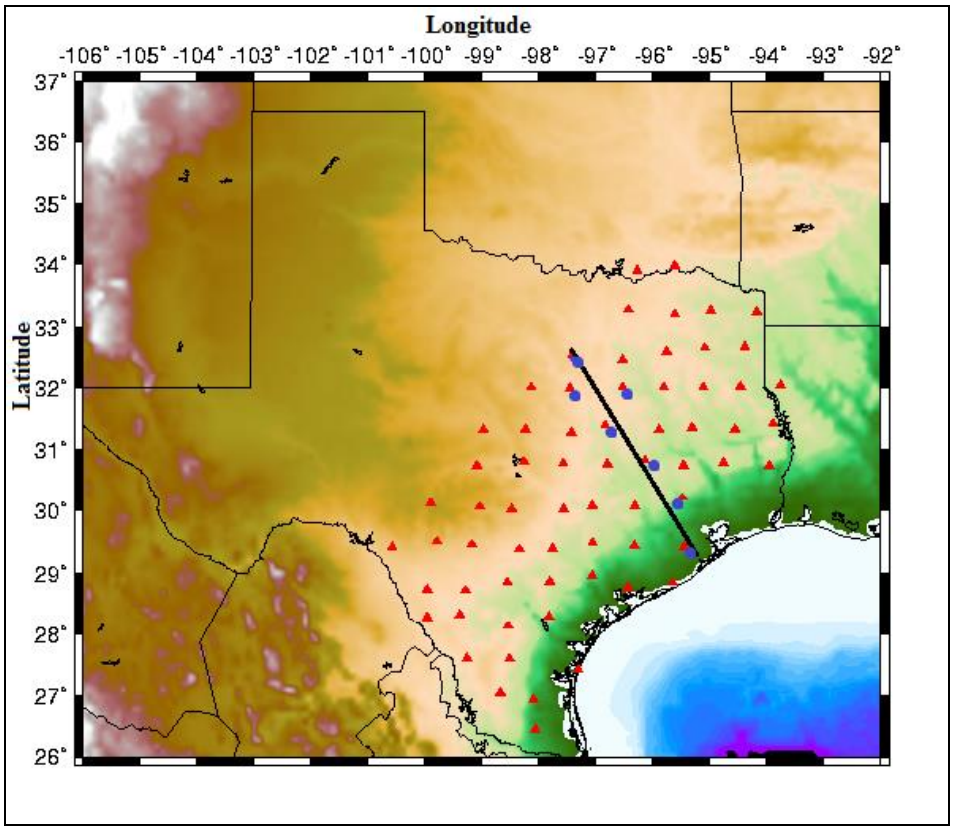

(a)

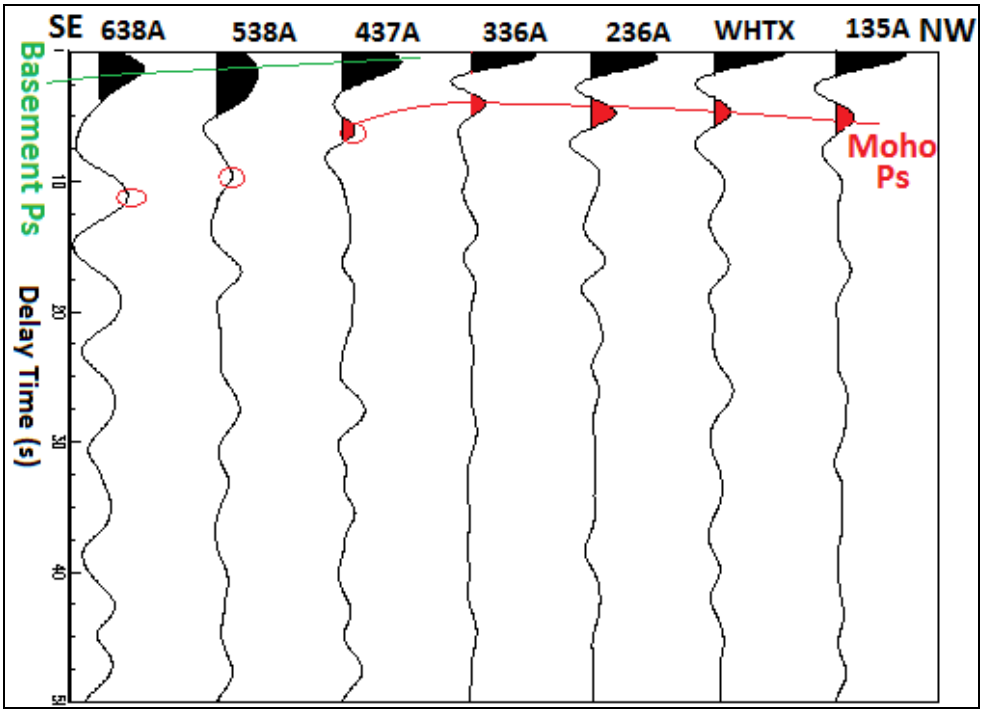

(b)

Figure 25. A profile of stacked receiver functions to the northern part of the study area: (a) the location of the profile. (b) Profile of stacked receiver functions of 7 stations trending from the coastal plain (southeast) to the Ouachita belt (northwest).

5.2 Results from H-κ Stacking Method

To compute the crustal thickness and V_p/V_s simultaneously, the H-κ stacking method of Zhu and Kanamori (2000) was applied for each station. An average crustal P velocity of 6.4 km/s was assumed for stacking. Crustal thickness and V_p/V_s are obtained from the location of s(H, κ) maximum, and uncertainties are also estimated according to the distribution of s(H, κ). This method worked successfully at stations in central Texas but failed at stations above thick sediments in the coastal plain since multiples from the top of the basement alter the primary Ps converted phase from the Moho. Results estimated from the H-κ stacking method are summarized in Table 1 and several examples are given below.

Table 1. Location of broadband stations and estimated Moho depth and V_p/V_s ratios estimated from both CCP and H-κ stacking methods

station	longitude	latitude	t_{ps} (s)	Moho Depth (km) (CCP)	H (km) (H-k)	V_p/V_s (H-k)
135A	-97.41	32.56	5	43.1	41.9±0.2	1.779±0.006
136A	-96.53	32.47	4.37	36.7	31.1±0.2	1.923±0.009
137A	-95.76	32.6	5.5	48.1	-	-
138A	-95.09	32.66	5	431	-	-
139A	-94.39	32.68	4.5	38.1	-	-
234A	-98.14	32	4.5	38.1	37.5±0.2	1.788±0.004
236A	-96.53	32	4.64	39.5	38.9±0.3	1.762±0.011
239A	-94.47	32.02	4.2	35.0	-	-
240A	-93.76	32.04	4.38	36.8	-	-
333A	-98.98	31.32	4.3	36.0	37.0±0.2	1.786±0.007
334A	-98.24	31.33	4.6	39.1	-	
335A	-97.43	31.28	5.2	43.1	-	-
336A	-96.84	31.39	4	33.3	46.6±0.2	1.532±0.004
433A	-99.09	30.75	4.6	39.1	41.0±0.1	1.701±0.002
434A	-98.27	30.81	4.58	38.9	37.4±0.1	1.811±0.004

435B	-97.58	30.78	5.2	45.1	33.4±0.1	1.989±0.005
533A	-99.04	30.07	5	43.1	-	-
534A	-98.48	30.03	5	43.1	41.6±0.1	1.881±0.003
535A	-97.57	30.03	5	38.1	34.4±0.2	1.862±0.008
631A	-100.58	29.41	4.5	35.0	34.4±0.1	1.798±0.005
632A	-99.79	29.51	6.2	55.2	40.6±0.3	1.944±0.011
633A	-99.18	29.46	3.8	31.5	36.0±0.1	1.973±0.005
634A	-98.35	29.38	5.8	43.1	-	-
732A	-99.97	28.73	4.3	36.8	-	-
733A	-99.29	28.72	5	43.1	-	-
734A	-98.56	28.85	5	43.1	-	-
832A	-99.97	28.28	3.9	32.4	-	-
833A	-99.39	28.32	4.5	38.1	-	-
933A	-99.27	27.61	4.9	42.1	47.6±0.3	1.562±0.005
WHTX	-97.46	31.99	4.8	41.1	41.5±0.2	1.753±0.004
Y37A	-95.62	31.98	5.25	45.1	-	-
Z36A	-96.43	33.27	4.8	41.1	-	-
Z37A	-95.62	33.2	4.9	42.1	-	-
Z38A	-94.99	33.26	5	43.1	-	-
Z38A	-94.99	33.26	5.5	43.1	-	-

*** t_{ps} stands for the delay time of Ps conversion phase from Moho; the red color marks the results that are considered as anomalies and will be discussed; "-" represents that no valid results exist at corresponding stations for H-κ stacking.**

Figure 26 and 27 display the H-κ stacking results at station 135A and WHTX. Colors from blue to red in Figure 26a and 27a represent increasing values of function s(H, κ). One clear maximum value of s(H, κ) is observed at both stations and corresponds to a crustal thickness of 41.9 km with a crustal V_p/V_s ratio of 1.78. The stacked receiver functions are shown in Figure 26b and 27b, on which both Ps and multiples from the Moho are clearly identified. In addition to the primary Ps phase, the multiples also contribute to s(H, κ) as described in the method section. Without constraints from multiples, H and κ can be traded off along the

moveout of Ps phase and no maximum of s(H, κ) can be detected. The Moho Ps arrival time at ~5s from the H-κ method agrees well with that from the CCP stack.

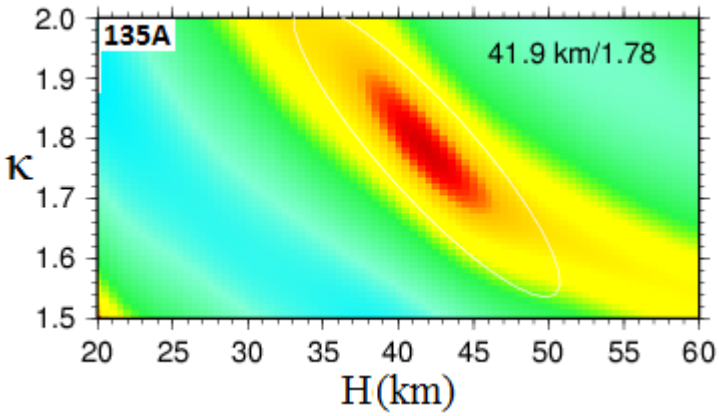

(a)

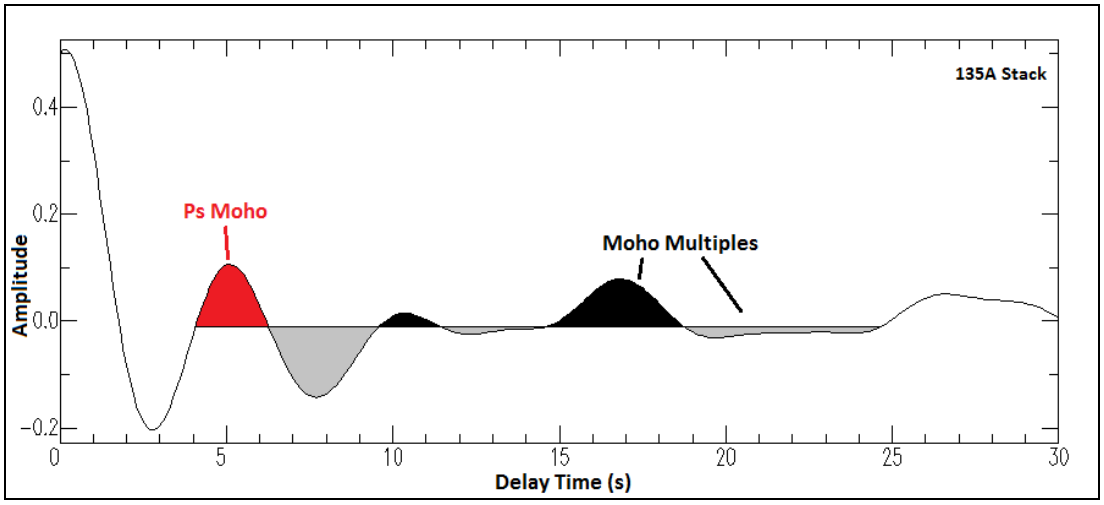

(b)

Figure 26. (a) The s(H, κ) for station 135A. The best estimation of the crustal thickness is 41.9 km with a V_p/V_s ratio of 1.78. The uncertainties are given by the ellipse. (b) Stacked receiver function and the predicted arrival time of Moho converted phases.

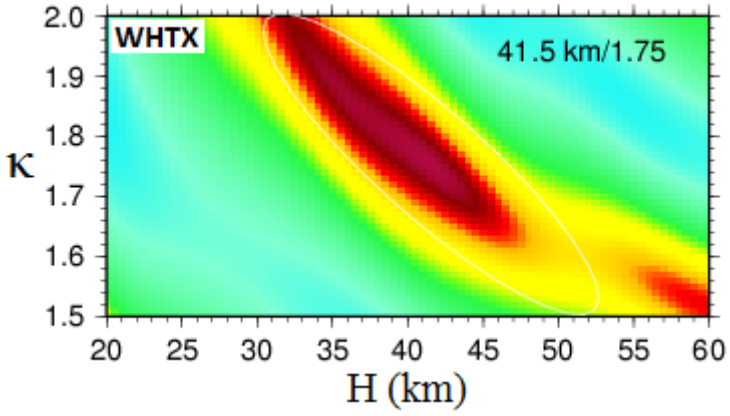

(a)

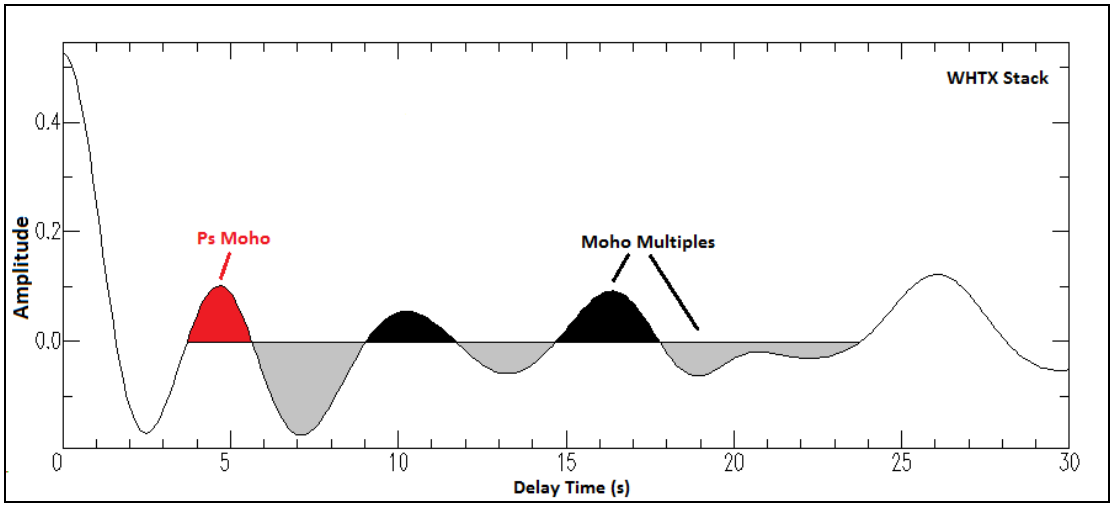

(b)

Figure 27. (a) The s(H, κ) for station WHTX. The best estimation of the crustal thickness is 41.5 km with a V_p/V_s ratio of 1.75. The uncertainties are given by the ellipse. (b) Stacked receiver function and the predicted arrival time of Moho converted phases.

Some H-κ stacking results show two maxima and cause ambiguity in determining crustal thickness and V_p/V_s ratio (Figure 28). This ambiguity could be attributed from other coherent phases such as Ps conversions from some upper mantle discontinuities or intracrustal multiples. The presence of these phases in s(H, κ) smears the maximum and cause other local maxima. In this case, information on the crustal thickness and V_p/V_s

ratio should be determined by referring to the nearby stations as suggested Zhu and Kanamori (2000). For station 336A, it is more reliable to pick the maximum approximating a crustal thickness of ~33 km with a V_p/V_s ratio about 1.79 rather than 46.6 km and 1.52 as appeared in Figure 28. The suggested combination of H and k would also agree more with the results from CCP stacking.

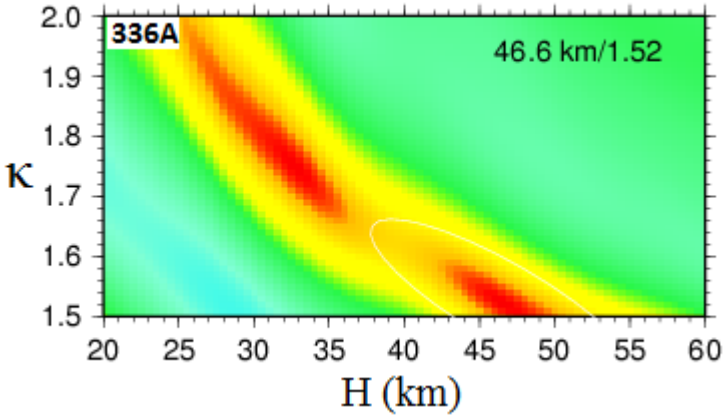

(a)

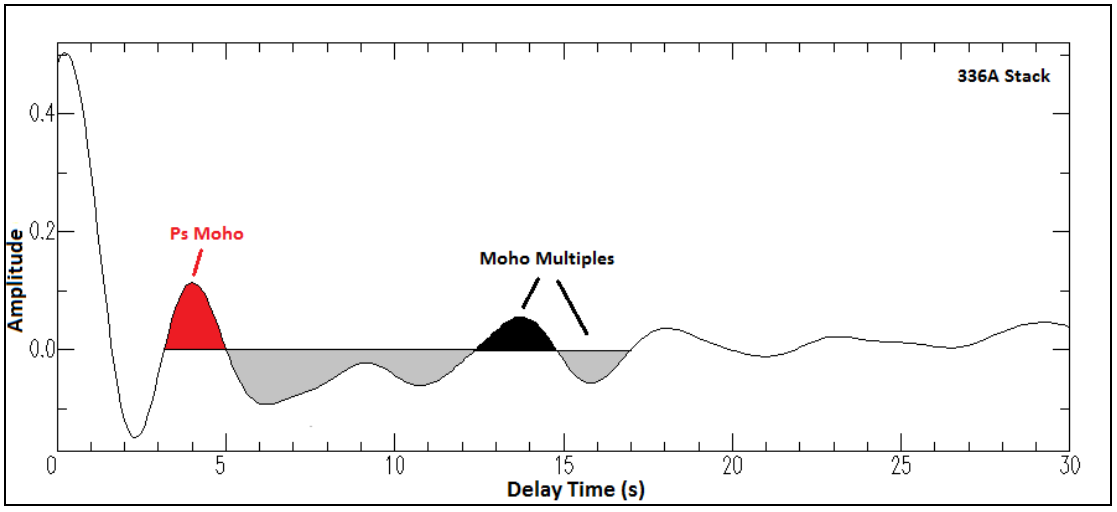

(b)

Figure 28. (a) The s(H, κ) for station 336A. The best estimation of the crustal thickness is 46.6 km with a V_p/V_s ratio of 1.52. The uncertainties are given by the ellipse. (b) Stacked receiver function and the predicted arrival time of Moho converted phases.

However, the H-κ results at some stations disagree with those derived from the CCP stacking methods (Table 1). For instances, at station 632A, which is located at the southern end of Ouachita belt, the H-κ stacking gives reliable values for crustal thickness of 40.6 km and a V_p/V_s ratio of 1.94 (Figure 29a), while the CCP stacking gives a crustal value of 55 km corresponding to a large delay time of 6.2 s for the Ps phase (Figure 29b). The discrepancy in the crustal thickness is due to the fixed V_p/V_s ratio (1.8) used in mapping the time on the CCP stack to depth. It can be seen on Figure 30a that the crustal thickness would be around 48 km for such a V_p/V_s ratio. In this case, the H-κ stacking method is more reliable than the CCP stacking. The high V_p/V_s here ratio may reflect geological information beneath the station, which will be addressed in the next section.

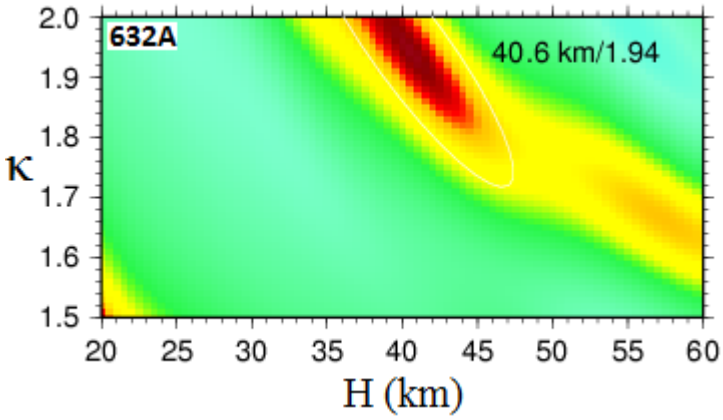

(a)

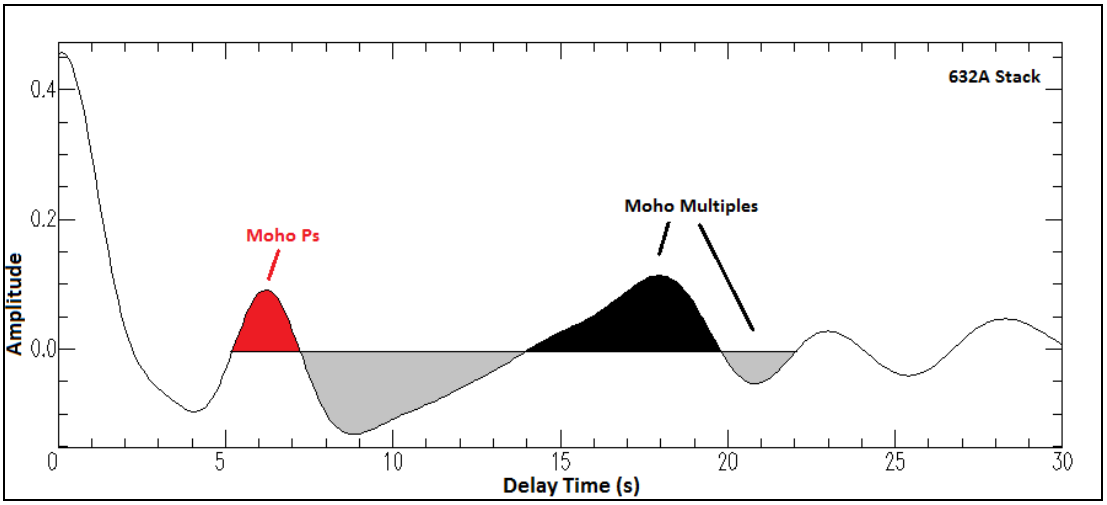

(b)

Figure 29. (a) The s(H, κ) for station 632A. The best estimation of the crustal thickness is 40.6 km with a V_p/V_s ratio of 1.94. The uncertainties are given by the ellipse. (b) Stacked receiver function and the predicted arrival time of Moho converted phases.

5.3 Moho Depth Variation of Southeast-Central Texas

The Moho depths derived from the CCP stacking and H-κ stacking method are plotted separately to produce continuous maps for Moho depth variation according to values in table 1 (Figure 30 and 31). The color scale is the same for both maps.

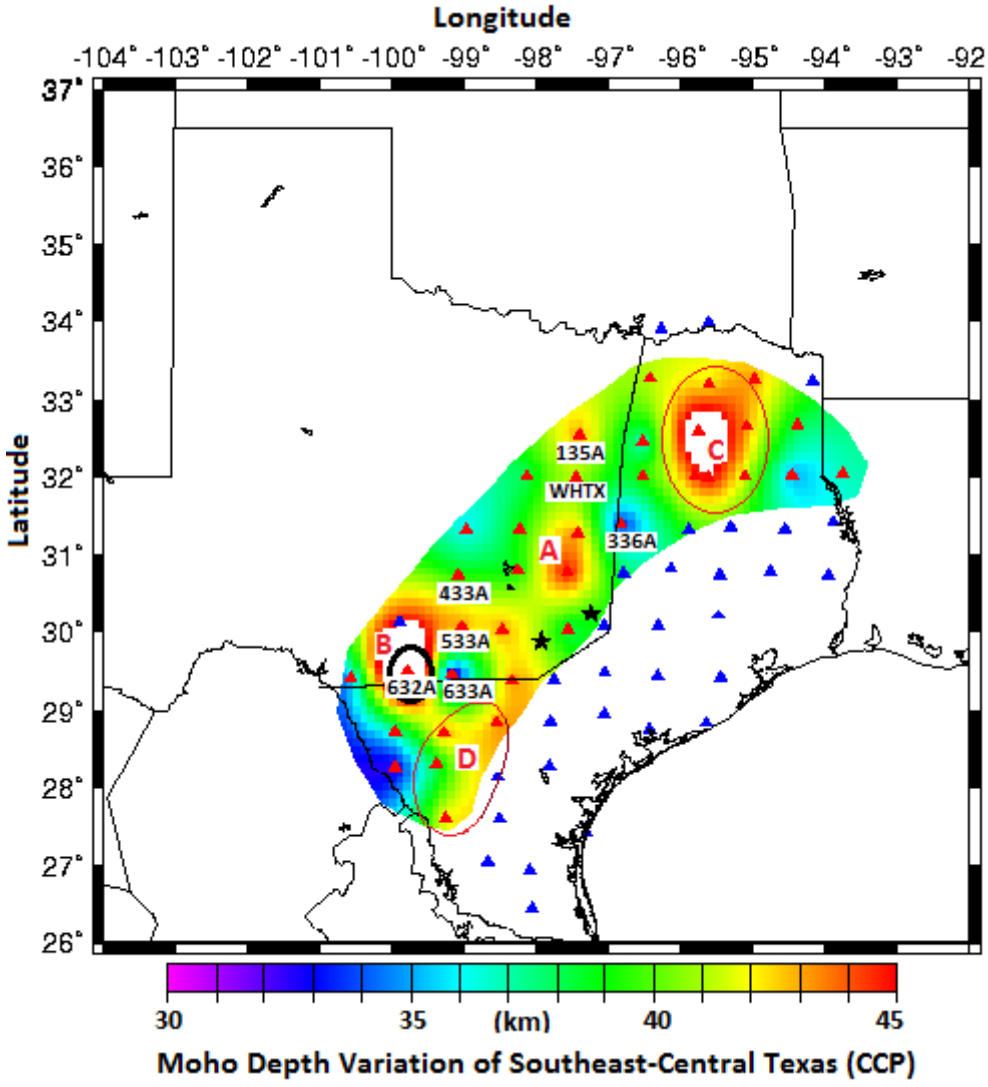

Figure 30. Moho depth variation of southeast-central Texas derived from CCP stacking method. Stations mentioned in the last sections are labeled; The Ouachita belt front is roughly outlined; Black stars denote San Marcos (south) and Austin (north), respectively.

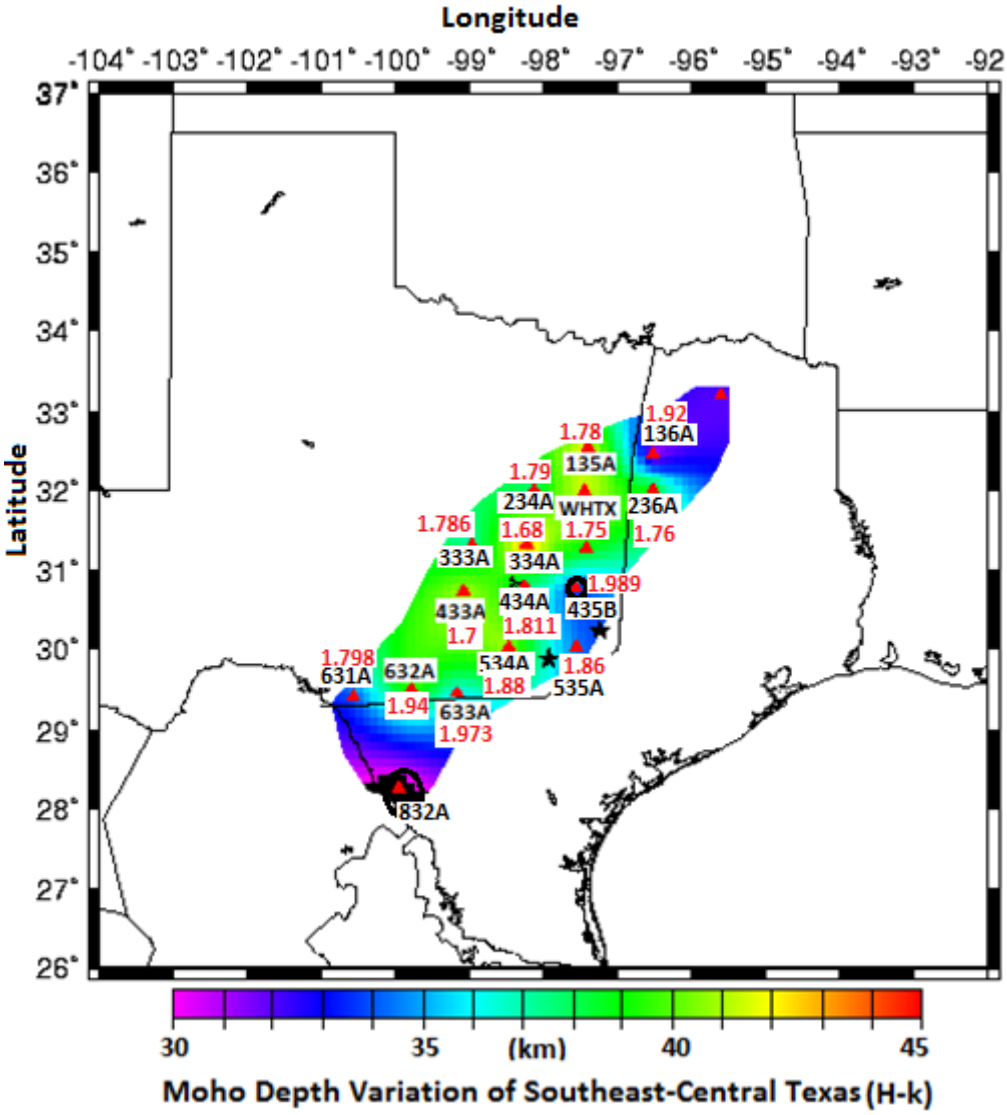

Figure 31. Moho depth variation of southeast-central Texas derived from H-κ stacking method. Stations are labeled; V_p/V_s ratios for each station are denoted in red. The Ouachita belt front is roughly outlined; Black stars denote San Marcos (south) and Austin (north).

On the map generated from CCP stacking (Figure 30), blue triangles stand for the stations that are used to generate receiver functions but fail to produce Moho depth. Only stations of red triangles are selected in plotting the maps. Crustal thickness from the H-κ stacking varies smoothly from approximate 40 km in the Llano uplift area in central

Texas to about 35 km near the edge of the Ouachita belt (Figure 31). The V_p/V_s ratio in the Llano uplift area is from 1.7 to 1.8, which is typical for continental crust (Zandt and Ammon, 1995; Zhu and Kanamori, 2000). High V_p/V_s ratios above 1.9 are imaged at stations close to the Ouachita belt, implying distinctive crustal formation beneath this area. The map from the CCP stacking is dominated by green color, corresponding to a 40 km thick crust, which largely agrees with the H-κ stacking. However, large and sudden variations in crustal thickness show on the map from the CCP stacking. For example, extremely thick crust of 55 km is obtained near the southern end of the Ouachita belt and in east Texas Basin. The causes of these anomalies are discussed below.

CHAPTER 6

DISCUSSION

6.1 Anomalous Moho Depth from the CCP Stacking

Anomalous thick crust is imaged on the map from the CCP stacking at several stations. Anomaly A is in the Llano uplift area, showing a Moho depth of ~45 km, which is probably reasonable for this region. Anomaly B is located near the southern end of Ouachita belt at station 632A, where a deep Moho of 55 km is obtained from a delayed Ps phase of 6.2s (Figure 29b). At both anomalous stations, the V_p/V_s ratios from the H-κ stacking (Figure 31) are high (1.989 and 1.94). As described above, these two anomalies could be attributed to inaccurate V_p/V_s ratio (1.73) used in the migration of the CCP stacks.

Another prominent anomaly on Figure 30 is in the northeast (anomaly C). Since this is in the east Texas basin, where no thick crust has been indicated from previous works, this apparent thick crust must not reflect the true structure. This anomaly is probably is probably caused by the interference of multiples from the base of sediments. In this case, the Ps conversion from the Moho mixed with multiples from shallow layers and result in an apparent delay in arrival time and a deep Moho. Similar anomalies are also recognized on the southern edge of Ouachita belt

(anomaly D), which should have the same origin as those appeared in the north. On the contrary, the inverted Moho depth from the H-κ stacking is around 35 km in this region and is more believable than that obtained by the CCP stacking. Nevertheless, only small confidence can be assigned to the estimation from the H-κ stacking in this area due to poor constraints from data.

Although the results from the CCP stacking depend heavily on the velocity model, it has an advantage in imaging the Moho depth using only Ps conversions when the H-κ stacking method fails due to the lack of coherent multiples. To obtain more reliable Moho depth from the CCP stacking, more realistic V_p/V_s ratios should be used in the velocity model. For areas covered by sediments or experienced volcanic activities, high V_p/V_s ratios are expected (Zandt and Ammon, 1995; Ahmed et al., 2013). The estimated Moho depth from the CCP stacking method would appear shallower if high V_p/V_s ratios are used. This would reduce the discrepancy between the results from the H-κ stacking and the CCP stacking methods.

6.2 The Ouachita Belt

The H-κ stacking result shows thinner crust and high V_p/V_s ratios about 1.9 for most stations along the Ouachita belt. The high V_p/V_s ratios may indicate the igneous material lying beneath this area that was generated by arc volcanic activities when the Paleozoic Ouachita orogeny was formed. Because the Ouachita Mountain is largely eroded and buried in central and southeast Texas, this finding provides new information for the Ouachita crust. It is interesting to notice that the crust along the belt is relatively thin compared to the Mesoproterozoic crust to its west. This is opposite to general cases that a thick crustal root is associated with ancient mountain belts (Fischer, 2002). However, it agrees with the opinion that the Ouachita orogeny was underlain by a subduction system that is characterized by a relatively shallow mantle rather than a crustal root (Huerta and Harry, 2012). The crust rocks beneath the Ouachita belt are probably dominant by mafic igneous rocks as suggested by high V_p/V_s ratios, which are denser than typical continental crustal rock. A thinner and denser crust beneath the Ouachita belt helps to explain the high Bouguer gravity anomaly band associated with the Ouachita orogeny (Figure 32).

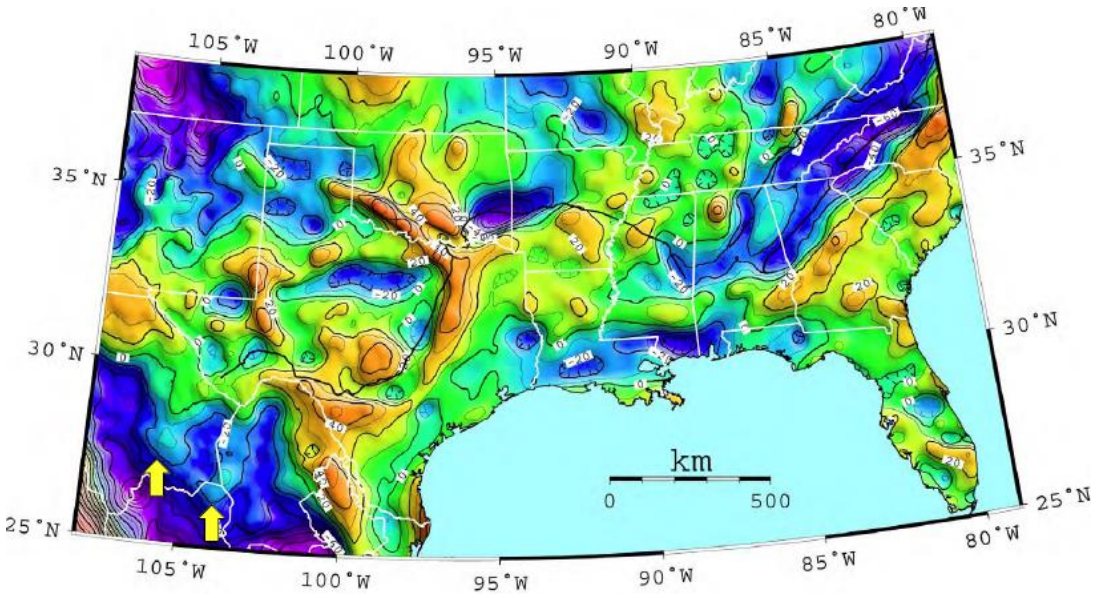

Figure 32. Bouguer gravity anomaly map of Texas. The high anomaly band is associated with the Ouachita orogeny (Keller, 2012).

6.3 Dipping Sedimentary Basement

Ps conversions from crystalline basement are observed at several stations located at the coastal plain area. The NW-SE profile in northeast Texas show increasing delay time of this Ps conversion towards the coast and indicate seaward thickening of the sedimentary layer. A dipping crystalline basement can also be shown from waveform variations of receiver function with azimuth. The example is given in Figure 24 for station 035Z, where the beginning part of individual receiver functions show dependence on back azimuth. The high amplitude P wave at zero time disappears on receiver functions associated with back azimuth between 140 °and 160 °(SE). The SE direction happens to be the dipping direction of the sedimentary basement (Laubach et al., 1990). In this case, the incoming energy approaches the basement from a nearly updip direction which cause the direct P wave to gradually decrease in amplitude on the radial component. The amplitude appears as the lowest when the impinging energy coincident exactly with the updip direction. As a result, the Ps converted phases from the basement appear as the apparent first arrival on the final resulted receiver function with a remarkable delay (Owens and Crosson, 1988). Therefore, the first arrivals with a time shift about 4s in Figure 24 could be interpreted as the outcome of a SE dipping sedimentary basement. On the other hand, the basement conversion on the receiver functions at larger back azimuth (~

300°) exhibit smaller delay time around 1.5s. However, the presence of the sharp velocity contrast in the shallow layer masks the arrivals from Moho and makes it difficult to determine the Moho depth.

CHAPTHER 7

CONCLUSIONS

Southeast-central Texas is an area with distinct tectonic features under the influence of Gulf of Mexico evolution. The investigation of deep structure of this area is important for the understanding of the tectonic inheritance and concurrent tectonic history of both Texas and Gulf of Mexico.

P-receiver functions were calculated for 117 events and 47 stations covering the Llano uplift in central Texas, the Ouachita orogenic belt, and the Texas coastal plain. P-receiver functions are stacked by using both the CCP and H-κ stacking methods. The CCP stacks show clear Ps conversion with delay time around 4-6s in central Texas, which corresponds to a Moho depth between 35 and 45km with an average of 40 km at most of stations. Anomalous thick crust is found at a couple of stations in the southern end of the Ouachita belt and in east Texas Basin, which turns out to be unreliable due to inaccurate velocity model used in mapping Ps arrivals to depth, while the anomalous stations show high V_p/V_s ratio from the H-κ stacking method. Results from the H-κ stacking method are more coherent and reliable in central Texas as both Ps and multiples are used to determine crustal thickness and V_p/V_s ratio. A large

uniform crustal thickness of 40 km is imaged in the Llano uplift area in central Texas with a typical V_p/V_s ratio of 1.7-1.8. Relative thin crust and high V_p/V_s ratio appear at stations in the Ouachita belt and its vicinity, indicating a more mafic origin of the crustal rocks, which makes sense for the Ouachita orogeny whose formation involved significant arc volcanic activities. High density of mafic rocks and the lack of crustal root beneath the Ouachita Mountain help to explain the observed high Bouguer gravity anomaly associated with the orogenic belt.

Most stations in the coastal plain area did not produce desirable receiver functions with good quality due to high noise level from the ocean and interferences from thick sedimentary layers. Despite the difficulty, a Ps conversion from the dipping crystalline basement is identified at some stations, indicating that the thickness of sediments increases toward the coast. Further waveform modeling of dipping interface between sedimentary layers and crystalline basement is needed in order to better map the variation of the sedimentary layer. Other techniques such as S receiver function or surface wave tomography might be used to image crustal thickness beneath the coastal plain.

References

Ahmed, A. et al., 2013. Crustal structure of the rifted volcanic margins and uplifted plateau of Western Yemen from receiver function analysis. Geophysical Research Abstracts, v. 15, EGU2013-13861.

Ammon, C., 1991. The isolation of receiver effects from teleseismic P waveforms. Bull. Seism. Soc. Am., v. l81, 2504-2510, 1991.

Bird, D. E., Burke, K., Hall, S.A., Casey, J.F., 2005. Gulf of Mexico tectonic history: Hotspot tracks, crustal boundaries, and early salt distribution. American Association of Petroleum Geologists Bulletin, v. 89, no. 3, doi: 10.1306/10280404026.

Bureau of Economic Geology, the University of Texas at Austin, 1997. Tectonic Map of Texas.

Carlson, W. D., Anderson, S. D., et al., 2007. High-Pressure metamorphism in the Texas Grenville orogeny: Mesoproterozoic Subduction of the southern Laurentian continental margin. International Geology Review, v. 49, p. 99-119. doi: 10.2747/0020-6814.49.2.99.

Colle, J. O., et al., 1952, Volumes of Mesozoic and Cenozoic Sediments in Western Gulf Coastal Plain of United States, Pt. 4 of Murray, G. E., Sedimentary Volumes in Gulf Coastal Plain of United States and Mexico, v. 83, p.1193-1200.

Cram, I. H., Jr., 1962, Crustal structure of Texas coastal plain region, American Association of Petroleum Geologists Bulletin, v. 46, p. 1721–1727.

Dickinson, W. R., 2009. The Gulf of Mexico and the southern margin of Laurentia. Geology, v.37, p.479-480, doi: 10.1130/focus052009.1.

Dunbar, J. A., and Sawyer, D.S., 1987. Implications of continental crust extension for plate reconstruction. An example from the Gulf of Mexico. Tectonics, v. 6, p. 739-755, doi: 101029/TC006i006p00739.

Fischer, K. M., 2002. Waning buoyancy in the crustal roots of old mountains Nature, v. 417, p. 933-936.

Garrison, J, R., 1981. Coal Creek serpentinite, Llano Uplift, Texas: A fragment of an incomplete Precambrian ophiolite. Geology, v. 9, p. 225-230.

Geissler, W., Plenefisch, T., et al., 2000. The Moho structure in western Eger rift: A receiver function experiment. Studia geoph. Et geod, v. 44, p. 188-194.

Harry, D. L., and Londono, J., 2004. Structure and evolution of the central Gulf of Mexico continental margin and coastal plain, southeast United States. Geological Society of America Bulletin, v. 116, p. 188-199, doi: 10.1130/B25237.1.

Houseknecht, D.W., 1986, Evolution from passive margin to foreland basin: The Atoka formation of the Arkoma basin, south-central U.S.A., *in* Allen, P.A., and Homewood, P., eds., Foreland basins: International Association of Sedimentologists Special Publication 8, p. 327–345.

Huerta, A. D., and Harry, D. L., 2012, Wilson cycles, tectonic inheritance, and rifting of the North American Gulf of Mexico continental margin: Geosphere, v. 8, p. 374-385, doi: 10.1130/GES00725.1.

Hynes, A., Rivers, T., 2010. Protracted continental collision — evidence from the Grenville Orogen.Can. J. Earth Sci, v. 47, p. 591-620, doi: 10.1139/E10-003.

Jackson School of Geoscience, the University of Texas at Austin, 2008. Map of Texas Basins.

Keller, G. R., and Shurbet, D. H., 1975, Crustal structure of the Texas Gulf Coastal Plain, Geological Society of America Bulletin, v. 86, p. 807–810, doi: 10.1130/0016-7606(1975)86<807: CSOTTG> 2.0.CO;2.

Keller, G. R., 2012. An Overview of the Structure and Evolution of the Ouachita Orogenic Belt from Mississippi to Mexico. Oral presentation a Tulsa Geological Society.

Langston, C. A., 1977. The effect of planar dipping structure on source and receiver responses for constant ray parameter. Bull. Seism. Soc. Am., 67, 1029-1050.

Langston, C. A., 1979. Structure under the Mount Rainier, Washington, inferred from teleseismic body waves. J. Geophys. Res., 84, 4749-4762.

Laubach, S. E., Jackson, M. L. W., 1990. Origin of arches in the northwestern Gulf of Mexico basin. Geology, v. 18, p. 595-598, doi: 10.1130/0091-7613(1990)018<0595:OOAITN>2.3.CO;2

Mickus, K., Stern, R. J., Keller, G. R., and Anthony, E.Y., 2009. Potential field evidence for a volcanic rifted margin along the Texas Gulf Coast. Geology, v.37, p.387-390, doi: 10.1130/G25465A.

Mohsen, A., 2004. A receiver function study of the crust and upper mantle across the dead sea transform. Doctoral dissertation, Free University of Berlin.

Mosher, S., et al., 2008. Mesoproterozoic plate tectonics: A collisional model for the Grenville-aged orogenic belt in the Llano uplift, central Texas, Geology, v. 36, p. 55-58, doi: 10.1130/G24049A.1.

Nicholas, R. L., and Rozendal, R. A., 1975, Subsurface positive elements within the Ouachita foldbelt in Texas and their relation to Paleozoic craton margin, American Association of Petroleum Geologists Bulletin, v. 459, p. 193–216.

Owens, T. J., Zandt, G., Taylor, S.R., 1984. Seismic evidence for an ancient rift beneath the Cumberland Plateau, Tennessee. A detailed analysis of broadband teleseismic P waveforms. J. Geophys. Res., 89, 7783-7795.

Owen, T. J., Crosson, R. S., 1988. Shallow structure effects on broadband teleseismic P waveforms. Bulletin of the Seismological Society of America, v. 78, p. 96-108.

Prewitt, R. H., 1969, Crustal thickness in central Texas as determined by Rayleigh wave dispersion (M.S. thesis), Lubbock, Texas Tech University, 69 p.

Raye, U., et al., 2011, Composition of the mantle lithosphere beneath south-central Laurentia: Evidence from peridotite xenoliths, Knippa, Texas Geosphere, EISSN 1553-040X, v. 7(3), p. 710–723.

Sodoudi, F., 2005. Lithospheric structure of the Aegean obtained from P and S receiver functions. Doctoral dissertation, Free University of Berlin.

Speckien, M., 2012. Magnetic Investigation of the Continental-Oceanic Crustal Boundary; Northern Gulf of Mexico. Master's Thesis, Baylor University.

Stewart, S. W., 1968, Crustal structure in Missouri by seismic-refraction methods, Seismological Society of America Bulletin, v. 58, p. 291-323.

Thomas, W. A., Viele, G. W., 1983. Tectonic history of the Ouachita orogeny, Geology, v.11, p.482-483, doi:10.1130/0091-7613(1983)11<482:THOTOO>2.0.CO;2

Thomas, W. A., 1991, The Appalachian-Ouachita rifted margin of southeastern North America, Geological Society of America Bulletin, v. 103, p. 415–431, doi: 10.1130/0016-7606(1991)103<0415:TAORMO>2.3.CO;2.

Yao, Y., 2013. Rayleigh wave tomography of Texas from ambient seismic noise. Master's Thesis, University of Houston.

Zandt, G and Ammon, C. J., 1995. Continental crust composition constrained by measurements of crustal Poisson's ratio. Nature 374: 152–154.

Zhu, L., 2000. Crustal structure across the San Andreas Fault, southern California from teleseismic converted waves. Earth and Planetary Science Letters, v. 179, p. 183-190.

Zhu, L., Kanamori, H., 2000. Moho depth variation in southern California from telesiesmic receiver functions. J. Geophys. Res., 105: 2969–2980.